Title of Thesis

Computational fluid dynamics investigation on performance and flow augmenting characteristics of a ducted marine turbine

A THESIS

SUBMITTED TO THE FACULTY OF THE

UNIVERSITY OF MINNESOTA DULUTH

BY:

Mohammad Arafat Zaman

IN PARTIAL FULFILLMENT OF THE REQUIREMENTS

FOR THE DEGREE OF

MASTER OF SCIENCE

IN MECHANICAL ENGINEERING

Dr. Craig Hill

Advisor, Assistant Professor, Mechanical & Industrial Engineering Department

July 2021

Acknowledgments

I would like to extend my greatest gratitude to my advisor, Professor Craig Hill, who has inspired my study of computational fluid dynamics focusing on renewable energy. He has provided excellent guidance throughout my studies and has allowed me to work on such an exciting project. I am very thankful for all the time and energy that he spent guiding me through this process, the words of encouragement that he gave me, and the knowledge that he was able to instill through his research experience. His passion for mentoring, scientific exploration and hard work will have a lasting impact on me far beyond my education at the University of Minnesota Duluth.

Furthermore, I would like to thank my committee members, Professor Venkata Menta and Professor Brock Hedegaard PE, for taking the time out of their busy schedules to assist me.

I would like to acknowledge the U.S. Department of Energy provided funding for this project through the Small Business Innovation Research (SBIR) grant and specifically Dennis Ramsey of SAHT Energy LLC in Eugene, OR for partnering with the University of Minnesota Duluth to explore the performance of the SAHT Energy marine turbine technology.

I would like to acknowledge the Marine & Atmospheric Observation and Energy Systems Lab at the University of Minnesota Duluth and Minnesota Super Computing Institute (MSI) at the University of Minnesota, who provided me with the High-Performance Computing resources used within this study.

Finally, I would like to express my gratitude to my family and friends for their unwavering support during this process. My graduate studies were made easier by their words of encouragement, support, and sincere interest in my study.

Dedication

This thesis is dedicated to my parents Anju Ara Begum and Mohammad Ansar Ali.

Abstract

The goal of this study was to investigate the flow augmentation and performance characteristics of SAHT Energy LLC's proprietary suction augmented hydrokinetic turbine (SAHT), which was designed to operate in shallower water, such as irrigation canals, and to transform the kinetic energy of flowing water into electrical energy. This research aimed to accelerate small business technologies in the marine hydrokinetic energy industry for the U.S. Department of Energy's SBIR (Small Business Innovation Research) program as a part of its Powering the Blue Economy initiatives. Suction augmented hydrokinetic turbine hydrodynamics and power performance characteristics were evaluated under various operating conditions and rotor configurations using the commercial simulation package Ansys Fluent (20.1) and high-performance computing (HPC) resources. The technology includes an axial-flow rotor contained within a funnel duct and a nacelle housed within a downstream converging-diverging nozzle that captures additional bypass flow and was hypothesized to augment near-wake pressure and velocity characteristics. Ongoing efforts focus on validating computational fluid dynamics (CFD) simulations against scaled-model flume experiments. Based on this numerical study, the highest power coefficient, $C_P = 0.31$, occurred with both five and seven bladed rotors using a NACA 64- series blade profile. The rotor and nacelle geometry proved to be the most efficient at λ =1.25 or 95 rpm. Because of a boundary layer separation from the sharp leading edge of the upstream funnel, the further installation of either just the upstream funnel or the funnel-nozzle combination was obstructing the flow through the rotor by lowering flow velocity inside of the SAHT unit. According to the simulation analysis, utilizing the funnel and nozzle geometry to augment hydrodynamics, the current SAHT unit design fails to increase efficiency compared to a design with a non-ducted rotor and nacelle. To ensure an improvement in power output and flow augmentation, future studies should examine the revised design of the funnel and nozzle configurations as well as the use of more valid rotor blade profiles. Validation of CFD modeling should also be performed, and perhaps some adjustments to CFD modeling based on the physical model analysis.

Table of Contents

List of Tables

List of Figures

Nomenclature Abbreviations and Acronyms

GHG	:	Greenhouse gas
WPTO	:	Water Power Technologies Office
PBE	:	Powering the Blue Economy
TWh	:	Terawatt hour or 1 trillion watt-hours
NYU	:	New York University
MHK	:	Marine Hydrokinetic
SAHT	:	Suction Augmented Hydrokinetic Turbine
LLC	:	Limited Liability Company
NACA	:	National Advisory Committee for Aeronautics
CFD	:	Computational fluid dynamics
RANS	:	Reynold's average Navier Stokes
URANS	:	Unsteady Reynold's average Navier Stokes
NS	:	Navier Stokes equation
TSR	:	Tip Speed Ratio
SST	:	Shear stress transport

List of Symbols

A	:	Rotor swept area, m^2
C_P	:	Coefficient of Power, unitless
C_T	:	Coefficient of Thrust, unitless
C_Q	:	Coefficient of Torque, unitless
R	:	Rotor radius, m
τ	:	Torque, N-m
F	:	Thrust, N
U	:	Undisturbed streamwise flow velocity upstream of the rotor, m/s
U_∞	:	Undisturbed streamwise flow velocity, m/s
U_x	:	Local streamwise velocity component, m/s
λ	:	Tip Speed Ratio, TSR, unitless
ω	:	Rotor angular velocity, rad/s
ωR	:	Rotor tip tangential velocity, m/s
ρ	:	Liquid water density, kg/m^3
μ	:	Dynamic viscosity of water, kg/ms
D_T	:	SAHT rotor diameter, m
D_F	:	Funnel opening diameter, m
D_N	:	Nozzle opening diameter, m
L_n	:	Nacelle length, m
L_F	:	Funnel length, m
L_N	:	Nozzle length, m
Z_h	:	SAHT hub height, m
η	:	Turbine rotor solidity

C_L/C_D	:	Ratio of the coefficient of lift divided by the coefficient of drag
R_{ij}	:	Reynolds stress tensor
$y+$	:	$y+$ is a non-dimensional distance and very important in turbulence modeling to determine the proper size of the cells near domain walls
I_U	:	Turbulence intensity, %

Section 1 - Introduction

Energy demand is increasing each day to satiate global energy consumption by a rapidly growing world population [8]. It is a controlling factor for several aspects of human life since almost all other production and consumption processes depend on energy supply [33]. Additionally, in the modern world, energy consumption is often proportional to an improved lifestyle and is crucial to the development and survival of human life [22]. A concern with increasing energy demand is the limited supply of fossil fuels which are currently the main source of energy production. Using fossil fuel also creates threats to the environment and human health by producing dangerous emissions such as greenhouse gasses (GHG) along with CO_2 and SO_2 [15]. Consequently, society faces an urgent necessity to adopt more sustainable energy resources to save our planet for future generations and not exhaust natural fossil fuels reserves [9]. As an alternative, renewable sources can provide sustainable power production for the future [6]. Sustainable renewable energy production can come from solar, thermal, bioenergy, hydro, tidal, wind, wave, and geothermal, among others and could contribute to routine energy consumption while offsetting some of the harmful impacts caused by burning fossil fuels [12,14]. Among these, energy from marine sources such as tides, waves, or ocean currents is one of the most unexplored areas among renewable energy sources on the planet [6].

The Water Power Technologies Office's (WPTO) Powering the Blue Economy (PBE) initiative, led by the US Department of Energy (DOE), is an essential step toward protecting, understanding, and leveraging immense power and promise of oceanic and riverine resources to accomplish various economic, social, and environmental goals. The PBE effort aims to better understand the power needs of expanding coastal and maritime industries, as well as improve technologies that might incorporate marine renewable energy to alleviate power limitations and allow for long-term blue economic expansion. In 2019, the DOE's WPTO produced the PBE report that thoroughly investigated potential markets using a set of common analyses: opportunity summary; application description and power requirements; market description, power options, and

geographic relevance; marine energy potential value proposition; and the path forward including research and development needs and potential partners [20]. One key discovery is that there are more potential markets both for power at sea (including ocean observation and navigation, underwater vehicle charging, marine aquaculture, marine algae, and seawater mining) and resilient coastal communities (including desalination, coastal resiliency, and disaster recovery, and community-scale isolated power systems) than previously thought [20].

In the United States, there exists a large potential to provide clean and renewable energy to communities within 50 miles of coastlines, which contains more than 50% of the total population. To estimate the full potential of future electricity production, three levels of resource assessment are being done by the WPTO to understand the potential contributions by the Nation's marine resources. Among the methods of theoretical, technical, and practical, the technical method explores the technical resource potential which implies the portion of the theoretically available annual average amount of physical energy that can be captured using a specific technology. The technical resource potential for energy generation from wave resources is estimated to range between 898–1,229 TWh/year, from tidal resources is estimated to range between 222–334 TWh/year, from ocean currents resources is estimated to range between 45–163 TWh/year, and from riverine hydrokinetic resources in the continental United States is 120 TWh/year [21]. The Electric Power Research Institute (EPRI) indicates that the total recoverable resource is around 10% of the current electricity demand in the U.S. [24].

Renewable energy production and distribution systems that are installed and controlled in marine environments are referred to as marine hydrokinetic (MHK) energy. This may include the technology of offshore wind, tidal stream, tidal range, river hydrokinetic, wave energy, ocean current, and ocean thermal, among others [13,2]. The process of harnessing kinetic energy from flow in different waterways such as rivers, oceans, or canals can be done in two ways either artificially creating dams in the pathway of water (i.e., conventional hydropower similar to that along the Columbia River in the Pacific Northwest, USA) or utilizing hydrokinetic turbines to extract energy. While creating dams alter the water environment and ecosystem around the blocked waterways,

MHK turbine technologies have less of an impact on the environment and ecosystem. MHK technologies can also be arranged in multi-unit arrays for hydropower generation from tidal and marine currents as opposed to tidal barrages where a basin's accumulated potential energy is harnessed. [16].

Modularity and scalability are important advantages of the hydrokinetic energy converter. Smaller-scale technologies can provide a cost-effective solution for areas that do not have access to electricity but are close to flowing water. These could support the goal to migrate away from fossil fuel-based energy supplies which contribute to greenhouse gas emissions, while also providing electricity for rural populations [17,25,35].

Significant technical, economic, operational, and environmental issues, among numerous other challenges, create large barriers for these emerging MHK technologies to move forward with commercial development. Optimizing turbine performance and deployment in arrays, balancing energy extraction with environmental impact, addressing socio-economic concerns, and resource assessment to determine annual energy yield and analysis of site characteristics are the main challenges in developing MHK energy conversion technologies. Additionally, emerging MHK technology developers often use improper cost projections in the early development stages due to an absence of empirical cost data, expensive market commercialization compared to the other forms of renewable energy (i.e., wind and solar), problems with technological lock-in because of expensive trial and error processes when sorting out viable designs and lack of commercial-ready designs available for energy providers to adopt. [17,19,24].

Several industries worldwide have deployed full-scale commercialized hydrokinetic turbine technologies. Unlike the wind energy industry, a single technology design does not dominate the MHK industry. MHK turbine technologies generally are categorized into either axial-flow or crossflow systems (Figure 1), depending on the orientation of the main power generation shaft rotation with the approaching flow.

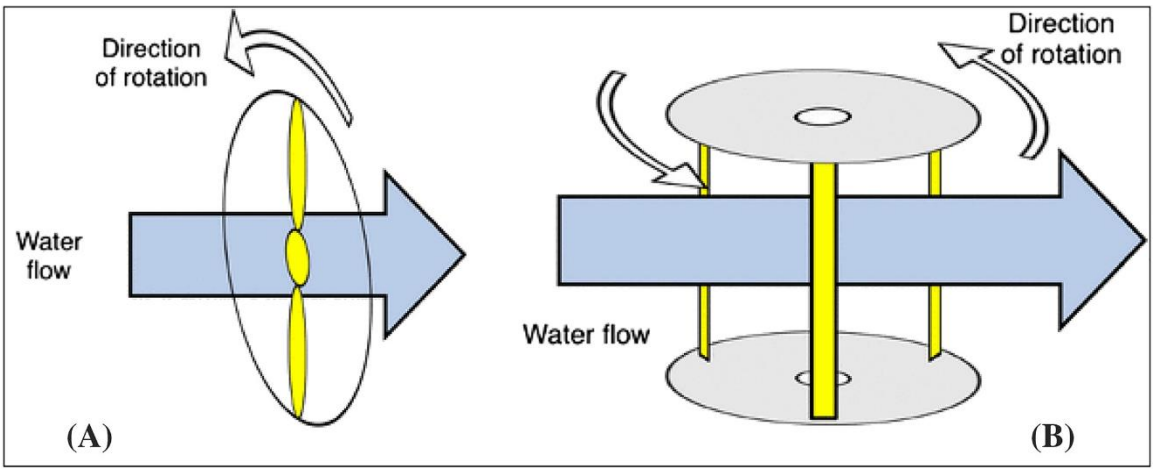

Figure 1: Schematic diagram of axial flow (A) and crossflow (B) MHK turbine [28]

The most active US axial-flow company is Verdant Power and they have tested six full-scale designs in the East River in New York City since 2006, making it the world's first commercially approved series of tidal turbines. On October 22, 2020, Verdant Power installed three Gen5 Free Flow System Turbines (Figure 2) on a TriFrame™ mount at the RITE Project [23].

Figure 2: Gen5 System Installation at RITE Project (Left) and Atlantis Energy's AR1500 tidal turbine (Right) [23,30]

The AR2000 (SIMEC Atlantis Energy), has been in development for over two years and builds on the achievements and lessons learned from the deployment and operation of AR1500 (Figure 2) on the world's leading MeyGen project in Scotland. An innovative new electro-mechanical pitch system, 360 degrees of yaw, upgraded onboard

health monitoring and diagnostics systems, and optimized redundancy of critical systems are featured on the AR2000 [30]. The AR2000 aims to have a 25-year design life with quarter-life interventions for routine maintenance. The SeaGen design of marine turbines was the first commercial-scale tidal generator in the world. Due to its horizontal support arm, the SeaGen is special and can be raised and lowered to allow the turbines to work above the water surface [30]. Although most MHK turbines have open tip blades, some designs adopt ducted marine turbines to exploit the hydrodynamic advantages of duct augmentation. For example, the open center ducted turbine design from OpenHydro places the generator along the circumference, eliminating a central shaft and shaft seal, and RER Hydro (Canada), or Renewable Energy Research, has developed the TREK (Kinetic Energy Recovery Turbine), a hydrokinetic turbine that harvests the power of river currents without the need for a dam as shown in Figure 3 [11,26,31].

Figure 3: The Open-Hydro PS2 ducted marine turbine (Left) and RER hydro (Canada) TREK ducted marine turbine (Right) [11,26]

SAHT Energy, LLC (Eugene, OR, USA) patented a power generation technology, a suction augmented hydrokinetic turbine (SAHT) which enables harvesting power by using the pressure force of water onto the face of the rotor while also channeling water behind the rotor to create suction, thus augmenting the power density. SAHT's turbine targets slower and shallower flows, and constricted flow spaces like irrigation canals. As

part of the US DOE's SBIR program, SAHT Energy was awarded Phase I funding to explore its hypothesis that the dual-ducted configuration augmented flow and increased operating efficiencies above that of a non-ducted version of its rotor. In this research, both hydrodynamic and power performance characteristics of the SAHT Energy technology are investigated to improve the unit's efficiency. The theory and working principles of MHK turbine energy extraction are discussed in Section 2. Numerical methods used for this study are discussed in Section 3, followed by Results in Section 4. The report concludes with a discussion of the results and recommendations for future research in Sections 5 and 6, respectively.

Section 2 - Characterizing Turbine Performance

2.1 The Betz limit and ducted turbine working principals

Reducing fluid flow velocity with little to no change in pressure as a fluid flows through the turbine rotor, open turbines can extract energy from the fluid. In Figure 4, the two outer lines are the streamlines, so mass should be conserved within those lines. In that case, the velocity increases through the rotor (the streamlines become closer together), and then the velocity decreases downstream in the wake (the outer streamlines expand away), indicating a lower velocity and large cross-sectional flow area to maintain continuity. Though to preserve continuity the streamlines must expand, but they cannot expand indefinitely. Therefore, a theoretical limit arises up to which the kinetic energy can be extracted from the fluid [18]. This limit has been shown by Betz to be 16/27 or 59.3% for a single actuator disk and is typically understood as a maximum upper limit for understanding the performance of non-ducted wind and marine energy technologies [7].

When a duct is added around the turbine (Figure 4), the expansion of the streamlines approaching the rotor is restricted by the duct geometry causing reduction of the downstream pressure. This increases the flow velocity across the rotor and results in a higher mass flow rate. The incorporation of a duct aims to redirect additional flow through the turbine and thus increase the extraction of available momentum. Moreover, a duct inhibits radial flow along with the blades of an axial flow turbine, and increased conversion efficiencies of up to about 90 percent can theoretically be attained. Energy is mainly derived by a reduction in pressure, so the turbine works more like an ultra-low-head hydro turbine than a traditional open tip non-ducted turbine [1,18].

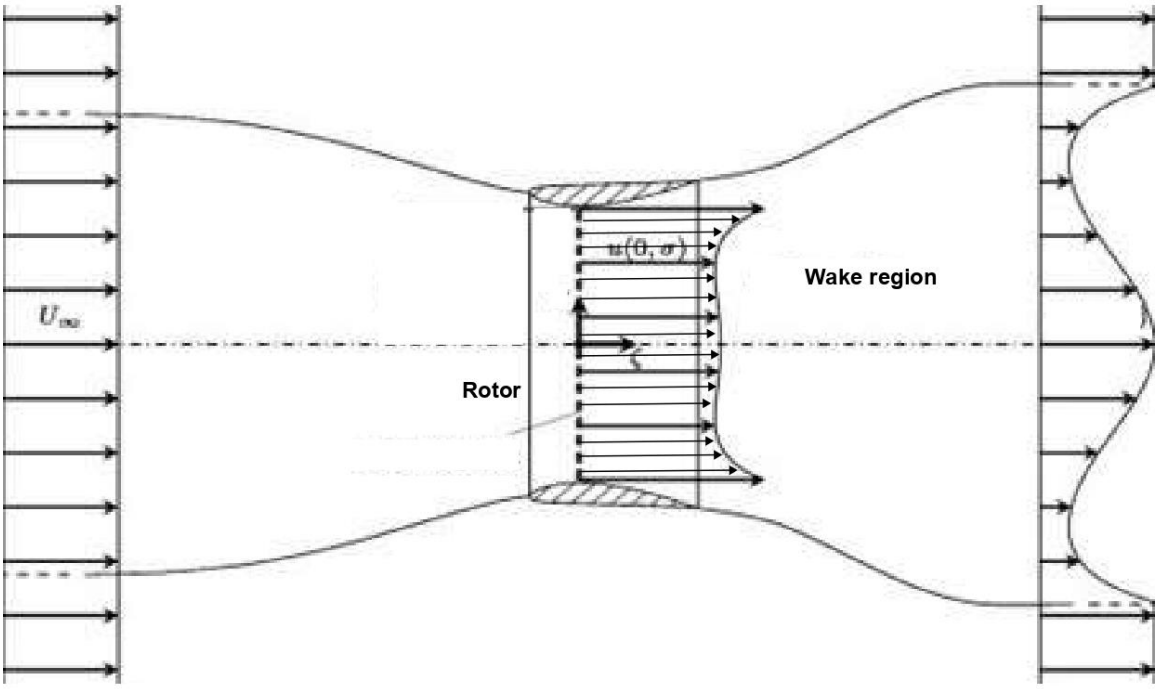

Figure 4: Schematic representation of a ducted turbine; the dense streamline indicates increased velocity through the rotor and the downstream expanded streamlines imply a decrease in velocity [10]

Riegler also showed theoretically, by diffuser-augmentation it is possible to accelerate the flow before the energy extraction, which allows gaining higher efficiency than the Betz limit [27].

Along with such hydrodynamic advantages of ducted turbines, there are several practical advantages in placing the turbine in a duct. Since a large diffuser duct reduces the downstream pressure, thereby increasing the available pressure drop, drawing in more flow, and increasing the power output of a given sized turbine then a smaller turbine can be used for power output. Additionally, the duct eliminates tip losses on axial flow turbine blades, improving efficiency. It also shades the turbine itself from direct sunlight and weed growth will thereby be reduced [18].

2.2 Performance characteristic equations

The primary parameters for the performance evaluation of a hydrokinetic turbine are the tip speed ratio (λ), power coefficient (C_P), torque coefficient (C_Q) and a thrust coefficient (C_T).

The power coefficient (C_P) is defined to determine the turbine hydrodynamic efficiency when the fluid free stream energy is converted into mechanical energy. The power coefficient (C_P) is defined as a ratio of mechanical rotational power achieved by the device ($\tau\omega$) and the overall mechanical power ($\frac{1}{2}\rho AU^3$) available to the device in the approaching flow.

$$C_P = \frac{2\tau\omega}{\rho AU^3} \tag{2.1}$$

Here, τ is the torque [Nm], ω is the rotational velocity of the rotor[rad/s], U is the undisturbed flow velocity upstream of the rotor [m/s], ρ is fluid density [kg/m^3], and A is the rotor swept area [m^2]. Both numerator and denominator have units of Watts.

The resulting thrust force on the device, in the streamwise direction; further contributes to the phenomenon of the fluid-structure interactions. This is quantified by the thrust coefficient (C_T) as a function of the thrust force on the system (F) and the overall thrust force ($\frac{1}{2}\rho AU^2$) theoretically induced over the region of the device.

$$C_T = \frac{2F}{\rho AU^2} \tag{2.2}$$

The stream-wise axial force on the unit is F [N].

The torque coefficient (C_Q) measures as a ratio of the mechanical torque obtained by the device (τ) and the maximum torque ($\frac{1}{2}\rho AU^2R$) theoretically acquired in the device region to produce the power.

$$C_Q = \frac{2\tau}{\rho AU^2R} \tag{2.3}$$

Here, R is the rotor radius [m].

As an analogy between the linear blade-tip velocity and the free-stream velocity, the tip-speed ratio (λ) is defined as:

$$\lambda = \frac{\omega R}{U} \qquad 2.4$$

Here, ωR is the tangential speed of the turbine's blade tip [m/s]. The above-mentioned parameters are critical to quantify during scaled experimental and computational studies as they enable similarity analysis and scaling studies for a full-scale system. This study focuses on these parameters to provide key information for SAHT Energy LLC as they seek to commercialize their turbine technology.

Section 3 - Numerical Setup and Computational Methodology

The turbine setup and hydrodynamic characteristics of this analysis are elaborated in the following sections, including the domain of the computational fluid dynamic (CFD) solver numerical setup and an explanation of the techniques used for the hydrodynamic and power performance CFD analysis.

3.1 SAHT Turbine Technology CAD Model

Simulations were performed to numerically recreate experimentation to achieve a validated CFD model for MHK turbine applications. A geometrically identical rotor, nacelle, funnel, and converging-diverging nozzle (herein referred to just as "nozzle") were utilized as shown in Figure 3. The entire unit comprises an upstream funnel, a downstream nozzle, an inside rotor which is the only rotating body, and a nacelle attached with the rotor's hub on the downstream side. The diameter of the SAHT rotor (D_T) is 0.189 m, the funnel opening diameter (D_F) at the upstream side is 0.282 m, and the nozzle upstream opening diameter (D_N) is 0.354 m. The length of the nacelle (L_n), funnel (L_F), and nozzle (L_N) - are 0.45 m, 0.55 m, and 0.65 m respectively. Both the rotor and nacelle are covered by the downstream nozzle. Additionally, the rotor is placed inside the upstream funnel. Three different geometry cases are shown in Figure 5.

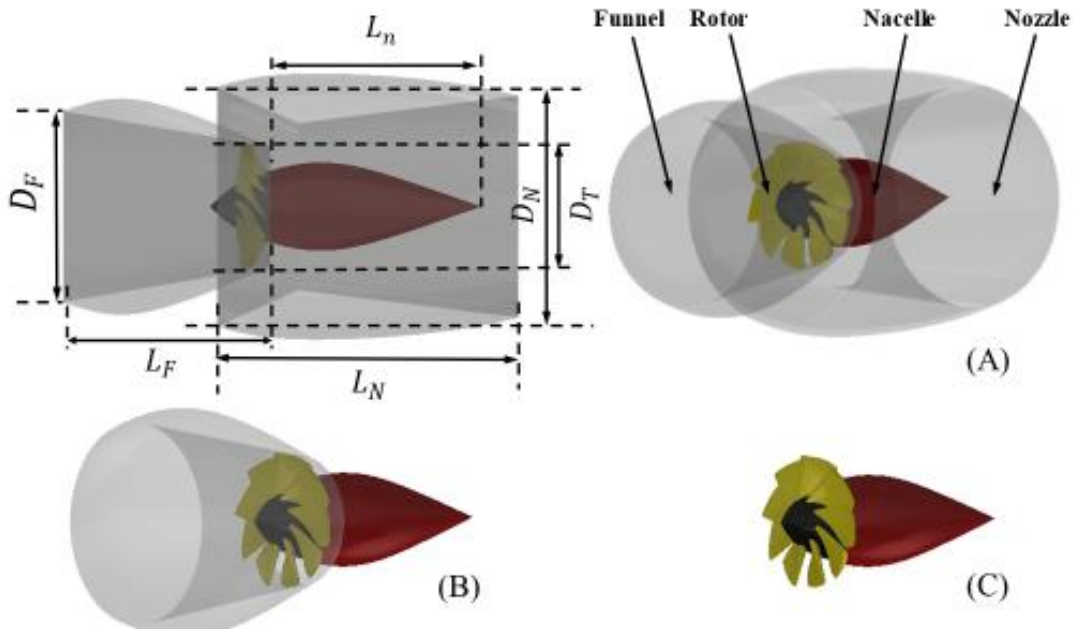

Figure 5: Geometrical model of the SAHT unit utilized for the CFD analyses. Full geometry test case (A); Rotor, nacelle, and funnel geometry test case (B); Only rotor and nacelle geometry test case (C).

Turbine rotor solidity (η) is known to influence the efficiency of a rotor. Solidity is essentially the total area of the blades divided by the total rotor swept area. Often times as solidity increases, tip-speed ratios of the optimal operating condition decrease, along with the maximum rotor efficiency. The fluid speed across the rotor plane is generally faster when there are fewer blades. When there are more blades, the torque may increase; however, it can reduce the fluid speed through the rotor. To achieve the best overall performance and efficiency, determining the optimal number of blades is important. In this study, four different configurations of the rotor are investigated, including 3, 5, 7, and 9 bladed rotors as shown in Figure 6.

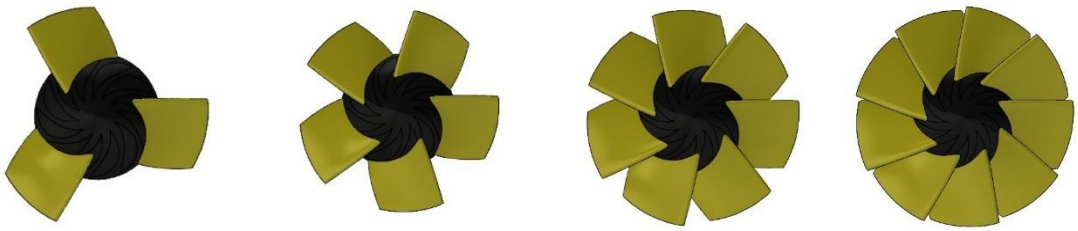

Figure 6: Different configurations of SAHT rotor. For all cases, the blades rotate counterclockwise. The rotor diameter (D_T), in all cases was 0.189m.

3.2 Blade Design

The initial blade design produced for the SAHT Energy turbine (Figure 7) rotor was inefficiently designed due to a sharp leading edge, very high angle of attack, non-optimized aerodynamic profile, and inversed high and low-pressure sides of the blade. The blade was redesigned using a common NACA (National Advisory Committee for Aeronautics) series blade profile shape with an optimized bend-twist configuration under two-dimensional flow conditions (Table 1). Blade designs were optimized prior to any knowledge of operating conditions or optimal tip speed ratio, so future efforts can further optimize the blade geometry.

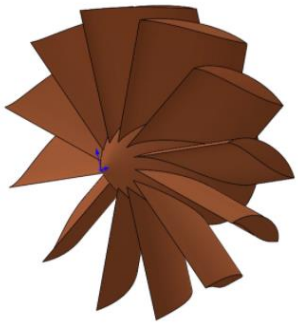

Figure 7: Previous inefficient rotor CAD model of SAHT unit

The NACA 64xx series blade has favorable lift and drag characteristics across a wide range of angles of attack and Reynolds numbers. The new blade design targeted a constant angle of attack along the length of the blade to operate at the peak of the C_L/C_D curve, approximately $\alpha = 6°$ (Figure 8). For structural reasons, a thicker blade profile was used near the root of the blade (NACA 6418 with 18% thickness ratio) compared to the tip of the blade (NACA 6414 with 14% thickness ratio).

Table 1: Blade geometry characteristics of the re-designed SAHT Energy blade. At the upstream leading edge of the blades, the diameter of the hub is 0.063m, so the blade begins its hydrodynamic profile at r/R = 0.33. Note that zero degree pre-twist would be parallel to the direction of approaching flow, and 90-degree pre-twist is parallel with the rotor plane of rotation.

r/R	R (m)	NACA Profile	Pre-Twist (degrees)	Chord length (m)
0.18	0.017	6418	32.24	0.073
0.35	0.033	6418	49.62	0.070
0.40	0.038	6418	53.44	0.069
0.45	0.043	6416	56.78	0.068
0.50	0.047	6416	59.70	0.067
0.55	0.052	6416	62.27	0.066
0.60	0.057	6416	64.53	0.065
0.65	0.061	6414	66.53	0.064
0.70	0.066	6414	68.35	0.063
0.75	0.071	6414	69.91	0.062
0.80	0.076	6414	71.34	0.061
0.85	0.080	6414	72.63	0.060
0.90	0.085	6414	73.80	0.059
0.95	0.090	6414	74.86	0.058
1.00	0.095	6414	75.83	0.057

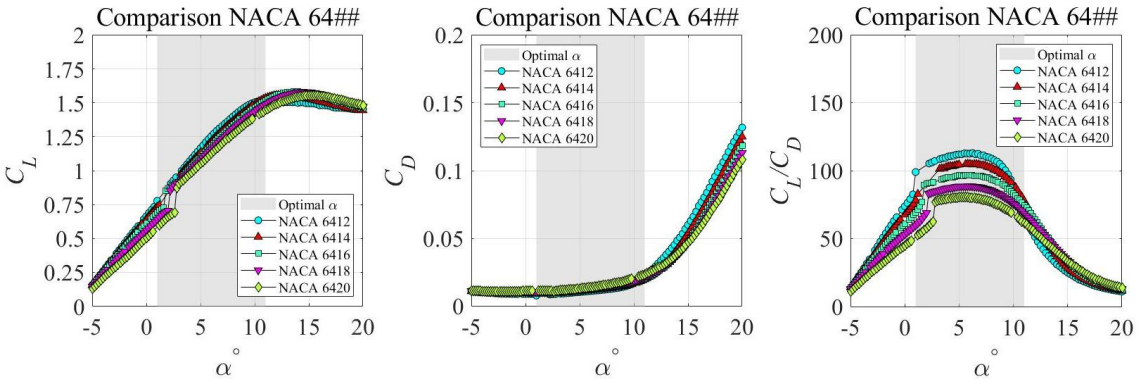

Figure 8: Aerodynamic force coefficients of the NACA 64xx series airfoils, used in the re-design of the SAHT Energy blade. The gray regions identify targeted operational angles of attack to maintain operation near the flatter peak regions of the C_L/C_D curves.

3.3 Computational Domain Details

The computational domain is shown in Figure 9 and is divided into three major domains: a rotational domain which encloses the rotor and itself is enclosed within a stationary refined fluid domain inside the funnel; a circular refined fluid region also incorporated from D_F = 0.282 m upstream to $5D_F$ = 1.41m immediately downstream of the rotor to capture the turbine outflow and wake characteristics, and the rectangular outer fluid domain with 1 m width and 0.8 m in depth. The outer fluid region (matched with scale model flume experiment which is out of the scope of this study) was sized $10D_F$ = 2.82 m upstream and $15D_F$ = 4.23 m downstream of the rotor. The turbine's hub height (Z_h), is 0.4 meters (Z_h/D_F = 1.42) above the floor, while the total water depth, d, is 0.8 meters (d/D_F = 2.84). The domain surrounding the SAHT rotor was segregated from the global domain to induce a moving-frame model with rotation at the turbine rotor relative to a stationary outer refined fluid domain, with interfaces between the two domains. Figure 9 shows a schematic of the numerical calculation domains, which comprise the turbine, nacelle, funnel, and nozzle.

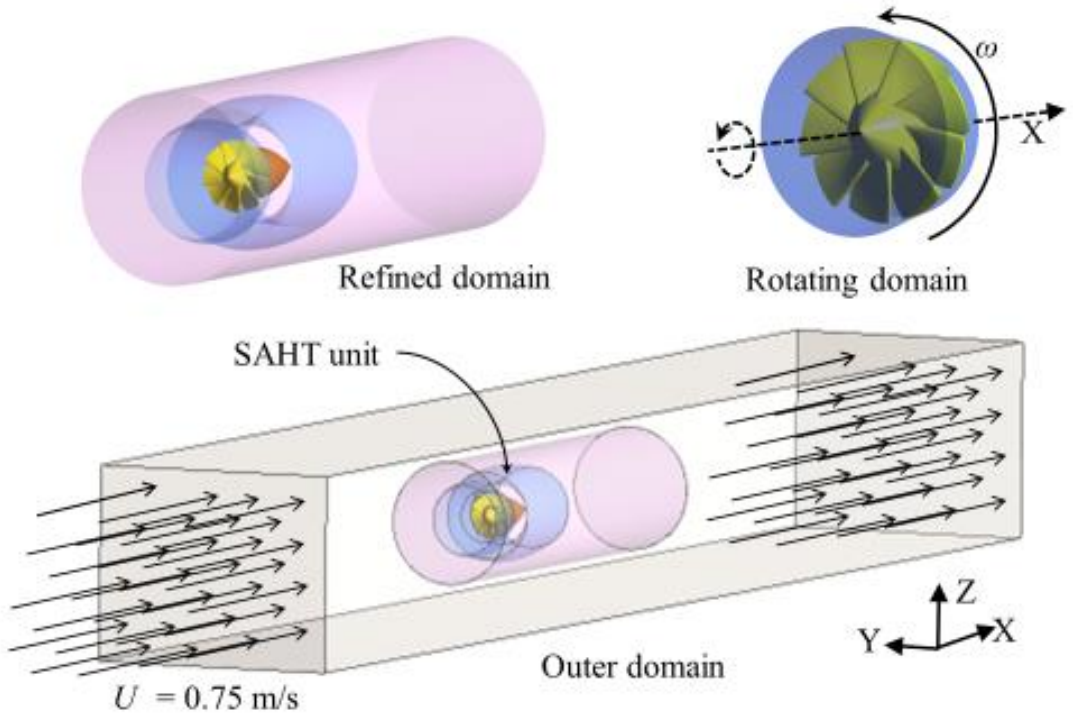

Figure 9: Geometry of computational domain. The simulated channel width was 1.0m with a depth of 0.8m. The SAHT rotor plane was located $10D_F$ = 2.82 m downstream of the inlet and $15D_F$ = 4.23 m upstream of the outlet. The cylindrical region near the turbine is the refined mesh region.

3.4 CFD Model Details

The CFD model used in this work is created with the commercial software program ANSYS Fluent (version 20.1), which solves the RANS equation using a finite volume approach. Since ANSYS Fluent is completely integrated with ANSYS Workbench and ANSYS Meshing, it can easily be used in conjunction with other ANSYS simulation technologies. The computational works of these simulations are done with the help of the University of Minnesota's high-performance computing (HPC), Minnesota Supercomputing Institute.

3.4.1 The Governing Equations

The ANSYS Fluent solver uses the finite volume methodology to solve problems. The governing equations are discretized and solved repeatedly across each sub-region using this methodology. As a result, the value of each variable is approximated at different locations throughout the domain.

The mass continuity equation (3.1) and the 3-dimensional (3D) Navier-Stokes (NS) equations (3.2-3.4), which are the governing equations solved by the ANSYS Fluent solver, and are written as:

$$u\frac{\partial \rho}{\partial x} + v\frac{\partial \rho}{\partial y} + w\frac{\partial \rho}{\partial z} + \frac{\partial \rho}{\partial t} = 0 \tag{3.1}$$

$$\rho\left(u\frac{\partial u}{\partial x} + v\frac{\partial u}{\partial y} + w\frac{\partial u}{\partial z} + \frac{\partial u}{\partial t}\right) = -\frac{\partial p}{\partial x} + 2\mu\frac{\partial^2 u}{\partial x^2} + \frac{\partial}{\partial y}\left(\mu\left(\frac{\partial u}{\partial y} + \frac{\partial v}{\partial x}\right)\right) + \frac{\partial}{\partial z}\left(\mu\left(\frac{\partial u}{\partial z} + \frac{\partial w}{\partial x}\right)\right) + F_1 \tag{3.2}$$

$$\rho\left(u\frac{\partial v}{\partial x} + v\frac{\partial v}{\partial y} + w\frac{\partial v}{\partial z} + \frac{\partial v}{\partial t}\right) = -\frac{\partial p}{\partial y} + 2\mu\frac{\partial^2 v}{\partial y^2} + \frac{\partial}{\partial x}\left(\mu\left(\frac{\partial u}{\partial y} + \frac{\partial v}{\partial x}\right)\right) + \frac{\partial}{\partial z}\left(\mu\left(\frac{\partial v}{\partial z} + \frac{\partial w}{\partial x}\right)\right) + F_2 \tag{3.3}$$

$$\rho\left(u\frac{\partial w}{\partial x} + v\frac{\partial w}{\partial y} + w\frac{\partial w}{\partial z} + \frac{\partial w}{\partial t}\right) = -\frac{\partial p}{\partial z} + 2\mu\frac{\partial^2 w}{\partial z^2} + \frac{\partial}{\partial x}\left(\mu\left(\frac{\partial u}{\partial z} + \frac{\partial w}{\partial x}\right)\right) + \frac{\partial}{\partial y}\left(\mu\left(\frac{\partial v}{\partial z} + \frac{\partial w}{\partial y}\right)\right) + F_3 - \rho g \tag{3.4}$$

where t is the time, ρ is the fluid density (kg/m^3), p is fluid pressure (Pa), μ is the dynamic viscosity (kg/ms), x, y, and z are Cartesian coordinates (as shown in Figure 9), the flow velocity in the x, y, and z directions are u, v, and w respectively, and the body forces on the fluid in the x, y, and z directions are F_1 , F_2 and F_3- ρg respectively. The mass continuity equation (3.1) implies that the rate at which mass enters a system is equal to the rate at which mass leaves the system plus the accumulation of mass within the system. For equation (3.2-3.4), the left-hand side contains the local and convective fluid acceleration terms, whereas the right-hand side includes forces due to pressure, gravity, and viscous shearing forces on the fluid. They are also known as equations of momentum conservation.

The turbulent flow shows some common flow characteristics such as irregularity, diffusive and dissipative nature, high Reynolds number, and 3D turbulent eddies. The NS equations can describe all kinds of fluid flow, yet a simpler version of it such as the Reynold average Navier Stokes (RANS) equations can efficiently deal with turbulent flows (as opposed to direct numerical simulation, which solves for all scales of turbulent flow yet is enormously computational expensive for high Reynolds number flows). The goal of Reynolds Averaging is to develop a set of equations to get an exact solution for the mean flow field. Since the mean flow field is often steady, we can develop steady-state solution approaches for the mean flow that require much less computational effort and resources than solving for the unsteady flow.

Any flow property quantity (e.g., Φ) of a turbulent flow field can be written as a summation of the mean value ($\bar{\phi}$)and a fluctuation value (ϕ') as shown in equation 3.5.

$$\Phi = \bar{\phi} + \phi' \tag{3.5}$$

The mean is defined by time averaging over a representative sampling period T:

$$\bar{\phi} = \frac{1}{T}\int_0^T \Phi \, dt \tag{3.6}$$

The sampling period is assumed to be long enough such that the random fluctuations average to zero:

$$\overline{\phi'} = \frac{1}{T}\int_0^T \phi' \, dt = 0 \tag{3.7}$$

For simplicity consider the incompressible NS equation with no body force, shown in equation 3.8.

$$\nabla \cdot \vec{V} = 0 \tag{3.8 (a)}$$

$$\rho\left[\frac{\partial \vec{V}}{\partial t} + \vec{V} \cdot \nabla\vec{V}\right] = -\nabla p + \mu\nabla^2 \vec{V} \tag{3.8 (b)}$$

Substituting the decomposed velocity components into the continuity equation gives:

$$\nabla \cdot [(\bar{u} + u')\hat{\imath} + (\bar{v} + v')\hat{\jmath} + (\bar{w} + w')\hat{k}\,] = 0 \tag{3.9}$$

Now upon time averaging and substituting in zero for the average of the fluctuating velocities, the equation reduces to Equation 3.10, which is identical in form to the original continuity equation.

$$\overrightarrow{\overline{V}} = \bar{u}\,\hat{\imath} + \bar{v}\,\hat{\jmath} + \bar{w}\,\hat{k} = 0$$
$$Or$$
$$\nabla \cdot \overrightarrow{\overline{V}} = 0 \qquad 3.10$$

However, when applying this time averaging procedure to the momentum equations, it results in Equation 3.11.

$$\rho\left[\frac{\partial \overrightarrow{\overline{V}}}{\partial t} + \overrightarrow{\overline{V}} \cdot \nabla \overrightarrow{\overline{V}}\right] + \rho \frac{\partial}{\partial x_j}\left(\overline{u_i' u_j'}\right) = -\nabla \bar{p} + \mu \nabla^2 \overrightarrow{\overline{V}} \qquad 3.11$$

Which includes the appearance of the additional term $u_i' u_j'$ representing the turbulent inertia tensor. This term cannot be neglected in a turbulent flow, and it is unknown.

The time-averaged momentum equation can be re-arranged as Equation 3.12.

$$\rho\left[\frac{\partial \overrightarrow{\overline{V}}}{\partial t} + \overrightarrow{\overline{V}} \cdot \nabla \overrightarrow{\overline{V}}\right] = -\nabla \bar{p} + \nabla \cdot \tau_{ij} \qquad 3.12$$

Where, τ_{ij} is described in Equation 3.13. This additional term is commonly known as Reynolds Stress Tensor (R_{ij}) which is shown in Equation 3.14 in tensor form.

$$\tau_{ij} = \mu\left(\frac{\partial \overline{u_i}}{\partial x_j} + \frac{\partial \overline{u_j}}{\partial x_i}\right) - \rho\left(\overline{u_i' u_j'}\right) \qquad 3.13$$

$$R_{ij} = \begin{matrix} \rho\overline{u'u'} & \rho\overline{u'v'} & \rho\overline{u'w'} \\ \rho\overline{v'u'} & \rho\overline{v'v'} & \rho\overline{v'w'} \\ \rho\overline{w'u'} & \rho\overline{w'v'} & \rho\overline{w'w'} \end{matrix} \qquad 3.14$$

The RANS equation set introduces nine new unknown variables, and to make the RANS equation well-defined the stress tensor components can be expressed by flow variables which introduce a challenge known as the Turbulent Closure Problem. Unlike the viscous stresses in the NS equations which are related to the strain rate, no exact solution physics-based approach exists for Reynolds stresses. The need to close the RANS

equations and this Reynolds stress tensor give rise to the art of turbulence modeling. There are various turbulence models such as k-ω, k-ε, Reynolds Stress 7 equation, among others. Among them the k-ω SST (shear stress transport) turbulence modeling is used in this study. It is a two-equation model which solves two transport equations along with the conservation equations. The two transported variables are turbulent kinetic energy (k), which determines the energy in turbulence, and specific turbulent dissipation rate (ω), which determines the rate of dissipation per unit of turbulent kinetic energy.

3.4.2 Mesh Characteristics

To identify an efficient size for the computing domain, a region mesh size dependence analysis was done. The total number of elements of computational domain gets more affected by the refinement of the solid surfaces in the rotating and refined domain. The effect of fluid domains cell size on the power coefficient and the number of total elements were first investigated by adjusting the fluid domain element sizes using the body sizing option in ANSYS meshing. The change in total number of elements of the computational domain was less than 1 million with the higher and lower limit of element sizes in the body sizing option. Body sizing of 0.05 m, 0.02 m, and 0.010 m were used for the outer fluid domain, middle refined fluid domain, and inner rotating domain respectively. Secondly, a mesh refinement on the solid surfaces of the rotor, nacelle, nozzle, and funnel was done by using an acceptable face element sizing of 0.0012 m and 0.0015 m on the rotor and nacelle surfaces respectively to capture all the curves and edges on the surfaces. Additionally, a face mesh refinement was done on the nozzle and funnel surfaces using 0.0035 m face element sizing. In order to capture the complicated geometry curvature and the small gap between faces efficiently, a global mesh control was incorporated using the curvature and proximity selection tab in ANSYS meshing. Figure 10 shows a closer look at the meshing around the SAHT unit. A grid dependency study, conducted to ensure the meshing is an efficient one with no compromise of the result, is shown in Table 2. Though the minimum number of elements is approximately 8M to achieve performance results accurately, 10M is selected to capture the geometry curvature

in a good manner. Table 3 shows the number of elements for different geometry and the number of blade configurations of the study.

Table 2: C_P comparison with number of CFD mesh elements (approximately), 1 million (M) = 10^6, Full geometry test case, 5 bladed rotor, λ = 1.25

Number of elements	$\boldsymbol{C_P}$
6 M	0.24
7 M	0.25
8 M	0.27
9 M	0.27
10 M	**0.27**
11 M	0.27

Table 3: Number of CFD mesh elements (approximately) comparison with different geometry and number of blades rotor configurations

1 million (M) = 10^6

SAHT unit setup	**3 blades**	**5 blades**	**7 blades**	**9 blades**
Only rotor & nacelle	4 M	5 M	5.5 M	6 M
Rotor, nacelle & funnel	6 M	7 M	8 M	9 M
Full Geometry	9 M	10 M	11 M	12.5 M

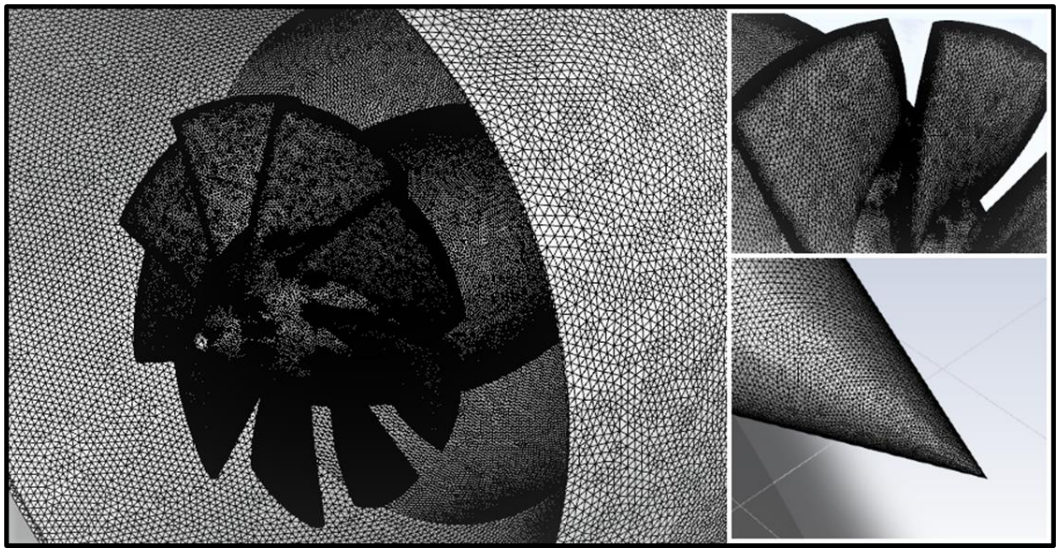

Figure 10: Geometric tessellation of surface meshing on the SAHT unit. Surface meshing on the rotor, nacelle, and the downstream nozzle is shown at left, a closer look at the rotor surface mesh (Upper-right) and rotor-tip surface mesh (Lower-right) are shown. The mesh size on these parts is so refined to accurately capture the curvature of the geometry and get more accurate results as well.

A schematic of the mesh, which shows the refinement around the turbine wall and support structure, can be seen in Figure 11:

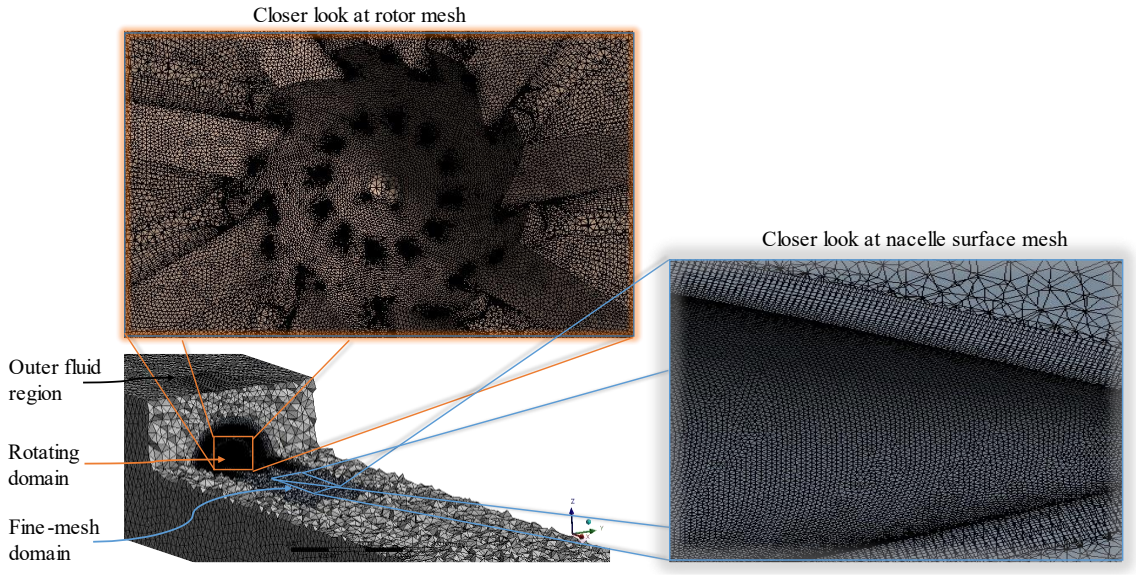

Figure 11: An illustration of the mesh that was utilized in the simulation, including the mesh refinement that was required.

3.4.3 Solver Physics Setup

All simulations were completed under steady-state conditions, not transient conditions. Transient simulations require many more computational resources. The scope of this project was to investigate the average hydrodynamic and performance characteristics of the SAHT technology, so steady-state RANS modeling appropriately achieved this goal. Unsteady (URANS) simulations could be used for future efforts if fluid-structure interactions or blade position resolved quantities are of interest. This, however, will require more computational effort since all domain mesh cells are solved at each time step. Steady-state RANS modeling optimizes the local time-step during simulations to more rapidly converge solutions.

The turbulence model used in these simulations is the k-ω SST. Liquid water is used as computational fluid with a constant density of ρ = 998.2 kg/$m^3$and a constant dynamic viscosity of μ = 0.001003 kg/m-s. The rotational speeds of the rotating domain

are defined by cell zone conditions which are changed depending on the different λ (range of 0.50 – 2.50) values. An inflow boundary condition is specified at one end of the outer fluid domain with an inflow velocity of 0.75 m/s and an outflow boundary condition, with a pressure specified at 0 Pa, at the other end. The inlet turbulence intensity was 5% and the turbulence-viscosity ratio was 10. No-slip wall conditions are instigated on the rotor, nacelle, funnel, and nozzle structures. At the outer domain, symmetry boundary conditions were used for the domain wall. The Coupled scheme is used for pressure-velocity coupling and second-order upwind was used for the spatial discretization of momentum, turbulence kinetic energy, and specific dissipation rate. The convergence requirement is 10^{-6} of the root mean square residual, however, to minimize the computational time 3000 number of iterations are incorporated with the simulation. The steady values of the residuals and performance coefficients coming after 1000 runs of simulations, justified the 3000 number of iterations to be enough. Figure 12 shows the residual convergence for one of the simulations with the k-ω SST turbulence model and the performance coefficients vs iterations graph is shown in Figure 13.

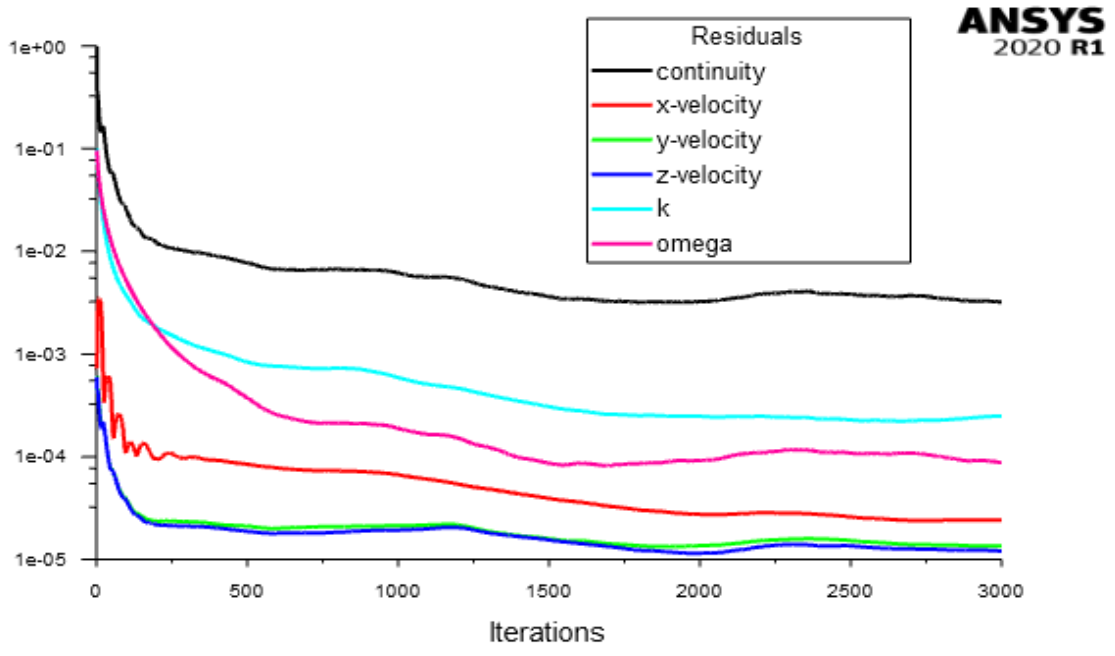

Figure 12: Residuals vs number of iterations plot; Full geometry; 5 bladed rotor; λ = 1.25

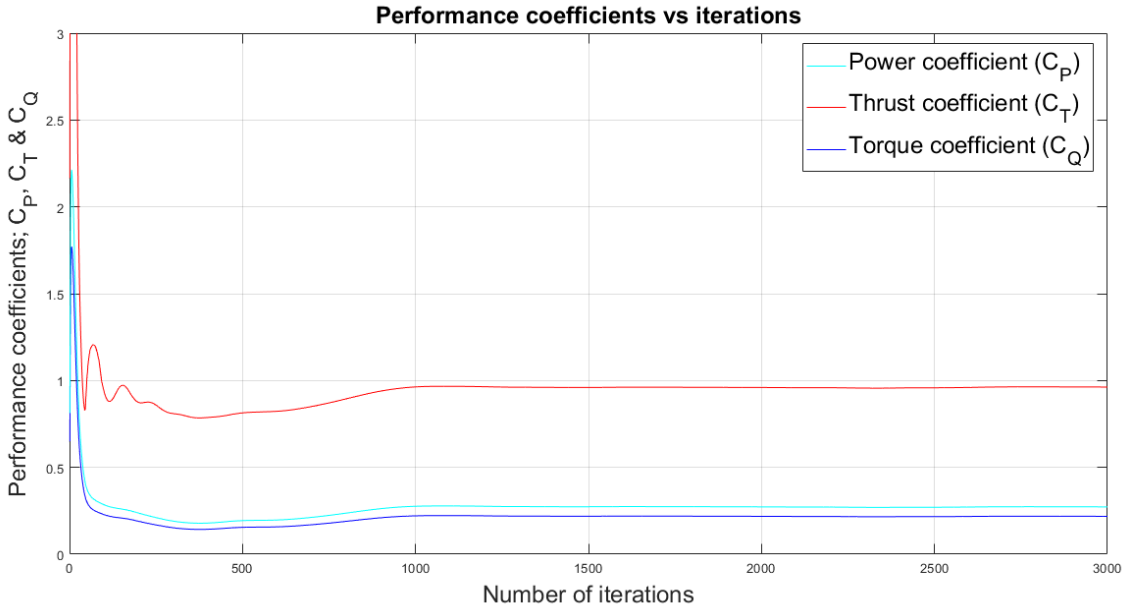

Figure 13: Performance coefficient vs iterations graphs; Full geometry; 5 bladed rotor; λ = 1.25. The performance coefficients are very steady and converge after approximately 1500 iterations.

3.4.4 Monitors

To monitor the parameters of pressure, velocity, and turbulent kinetic energy two plane and two-line monitors were incorporated as below (Table 4) and shown in Figure 14:

Table 4: CFD parameter monitors

Monitor	Location
Horizontal Plane Monitor	from inlet to outlet and the full width of domain
Vertical Plane Monitor	from inlet to outlet and the full height of domain
Point Monitor	(x, y, z) = (-3D_F, 0, 0)
Central Line Monitor	(x, y, z) = (-5D_F, 0, 0) to (10D_F, 0, 0)

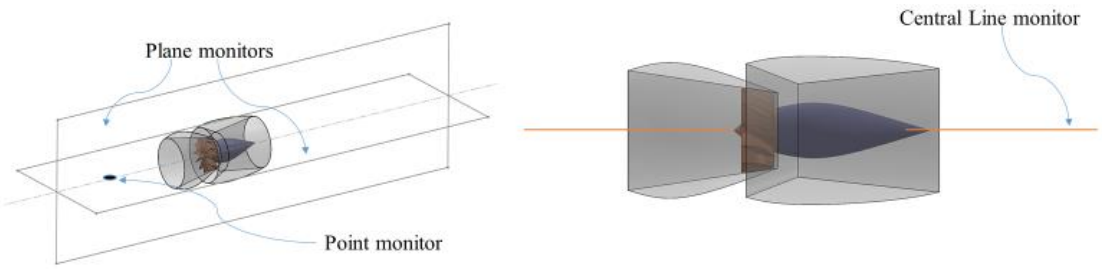

Figure 14: Representation of CFD monitors (Plane and Line monitors)

Surface mapping of y^+ value and normalized pressure on rotor, nacelle, nozzle, and funnel were also used. Finally, the torque and thrust on the rotor were calculated from the simulation, and with the help of characterizing equations the coefficients of power, thrust and torque were determined.

Section 4 - Results

4.1 Power Coefficient (C_P)

The torque on the rotor is calculated numerically and the power coefficient (C_P) curves are established by Equation 2.1. Among the three different geometry cases investigated, the maximum C_P values occurred with only the rotor and nacelle geometry cases and minimum C_P values occurred with the rotor, nacelle, and funnel geometry cases for all blade configurations. The maximum C_P=0.31 occurred for both five and seven-bladed rotors with the rotor and nacelle test case at λ =1.25. The C_P values gradually increase up to λ =1.25 and then drop down with further increasing TSR. The C_P comparison among the blade configurations and geometry cases is shown in Figure 15.

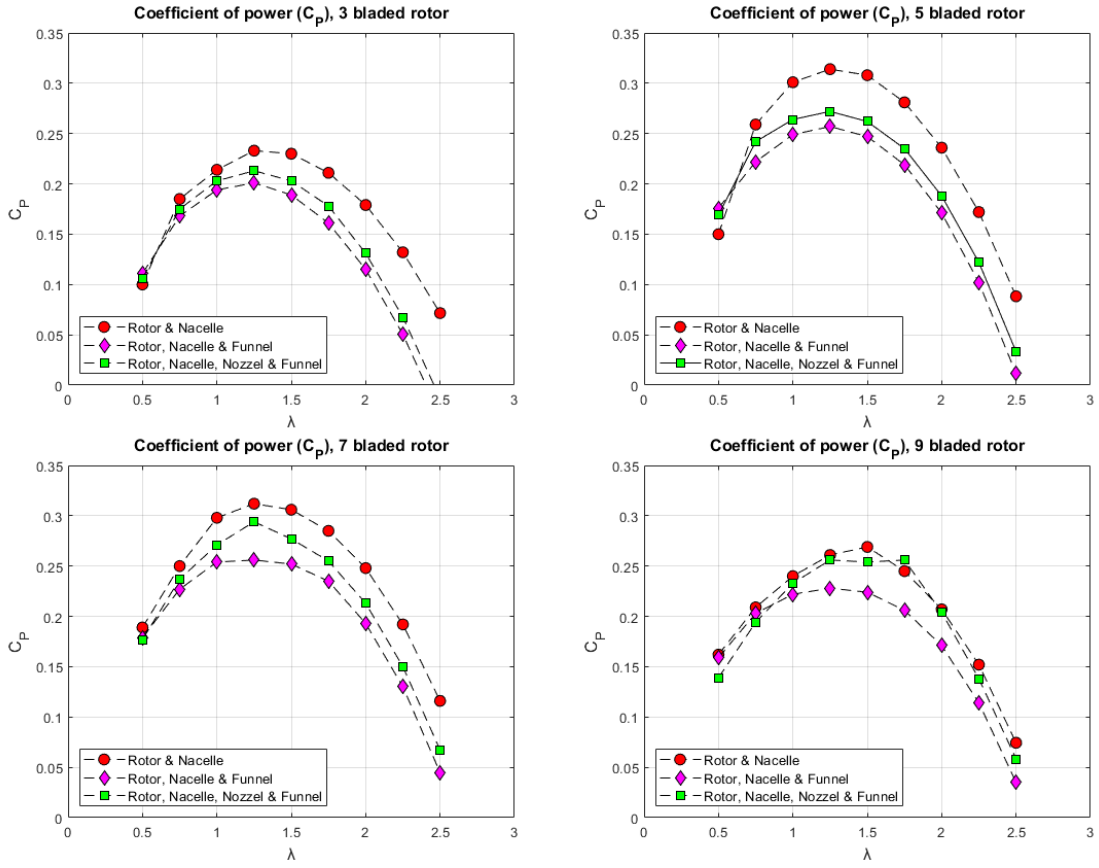

Figure 15: Power coefficient (C_P) vs. tip speed ratio (λ) comparing the power coefficient for the 3 bladed rotor (upper-left); 5 bladed rotor (upper-right); 7 bladed rotor (lower-left); and 9 bladed rotor (lower-right).

4.2 Thrust Coefficient (C_T)

Similarly, the thrust on the rotor is calculated numerically and the thrust coefficient (C_T) curves are established by Equation 2.2 for four different numbers of blade configurations and three separate geometry cases for each of the blade configurations. C_T values came out as maximum for the full geometry cases (rotor, nacelle, funnel, and nozzle) and they are gently dropping down with increasing λ value. The C_T comparison among the blade configurations and geometry cases is shown in Figure 16.

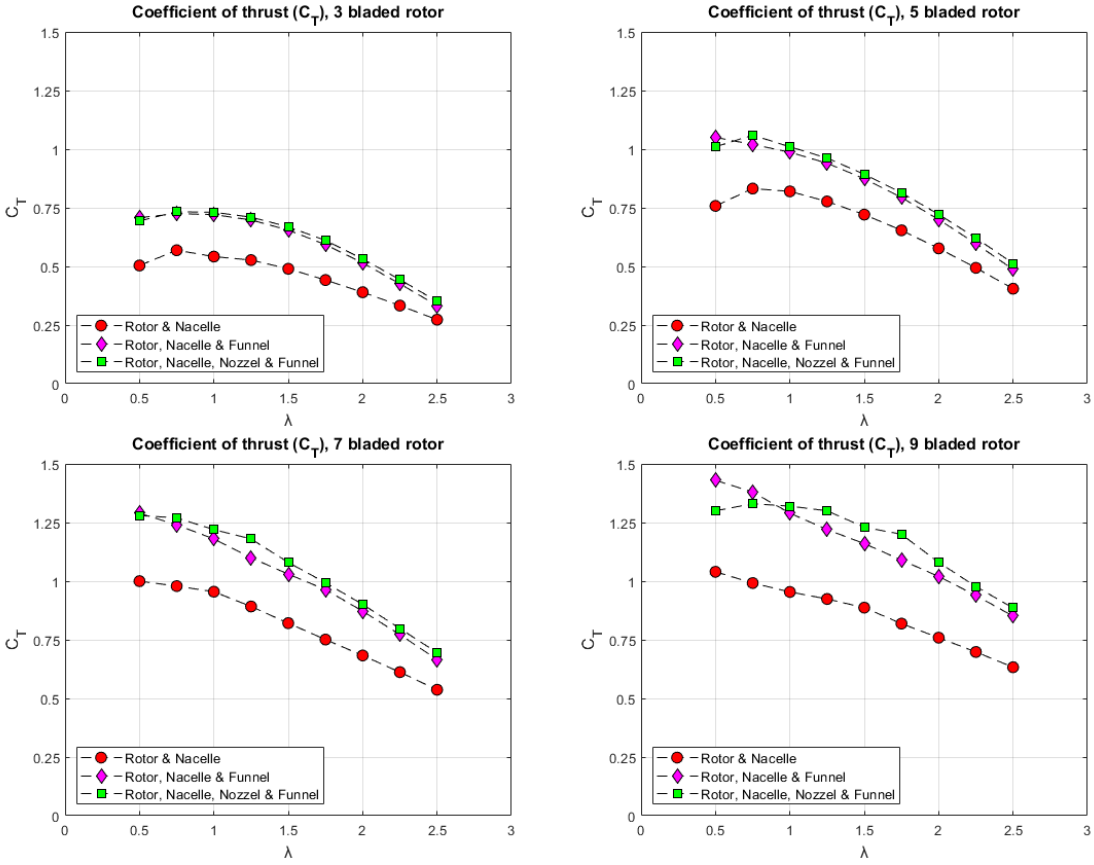

Figure 16: Thrust coefficient (C_T) vs. tip speed ratio (λ) comparing the thrust coefficient for the 3 bladed rotor (upper-left); 5 bladed rotor (upper-right); 7 bladed rotor (lower-left); and 9 bladed rotor (lower-right)

4.3 Torque Coefficient (C_Q)

Torque coefficient (C_Q) Curves for four distinct number of blade configurations and three distinct geometry scenarios for each of the blade configurations are produced using Equation 2.3 and numerically determined torque on the rotor. Similar to the thrust coefficient, the C_Q values are gently decreasing with the increasing λ value for all geometry cases and the number of blade configurations. And similar to the power coefficient, maximum C_Q values occurred with only the rotor and nacelle geometry cases and minimum C_Q values occurred with the rotor, nacelle, and funnel geometry cases for all blade configurations. Figure 17 shows the (C_Q) comparison of the blade configurations and geometry situations.

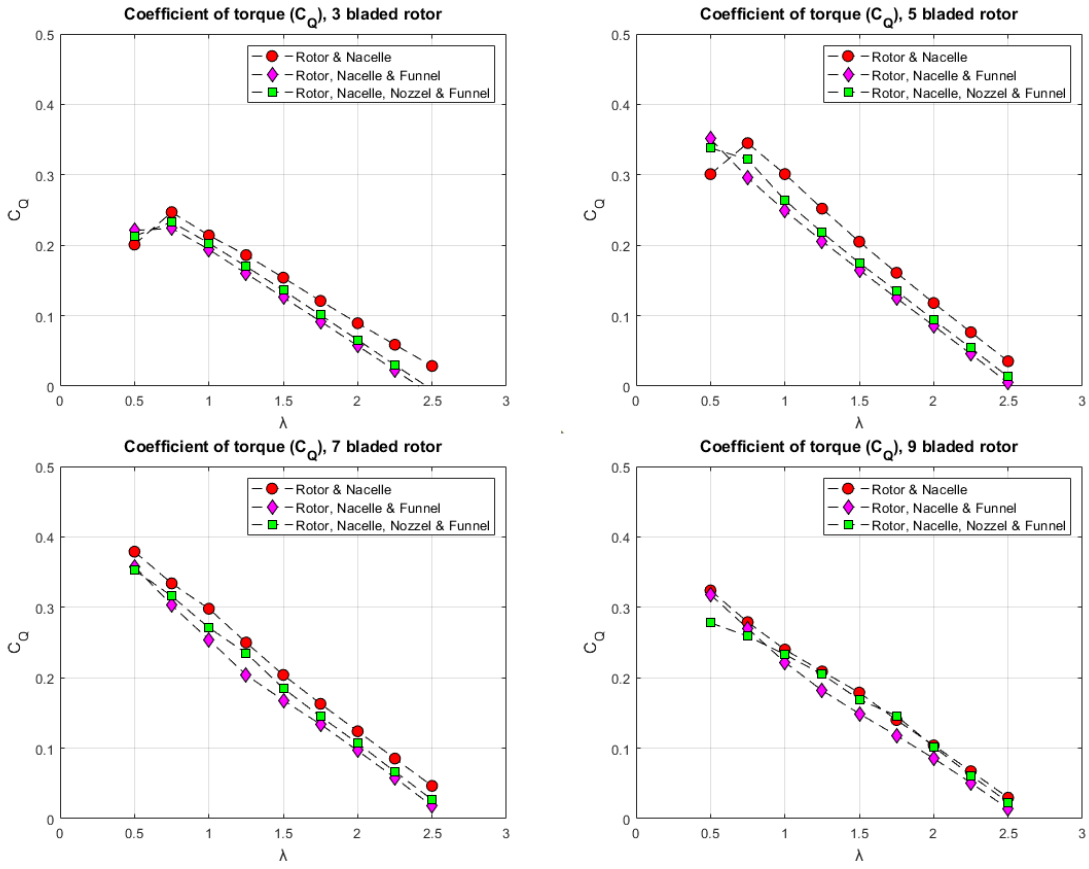

Figure 17: Torque coefficient (C_Q) vs. tip speed ratio (λ) comparing the torque coefficient for the 3 bladed rotor (upper-left); 5 bladed rotor (upper-right); 7 bladed rotor (lower-left); and 9 bladed rotor (lower-right)

4.4 The Optimal Number of Blades and Optimal λ

Depending on the numerically achieved power coefficient (C_P) for four configurations of blades and three distinct geometry cases of SAHT unit, 5 number of blades is treated as an optimal configuration to produce power. Though for some cases, 7 number of blades configuration achieved a little higher C_P value than 5 number of blades but considering the cost of manufacturing and a negligible increase in C_P values, 5 number of blades would be the best choice for the current SAHT unit. And from the numerically calculated C_P values for the different number of blades and geometry configuration, TSR 1.25 turned out as the optimal λ for the current SAHT unit under current operating conditions. Figure 18 represents the whole scenario about these.

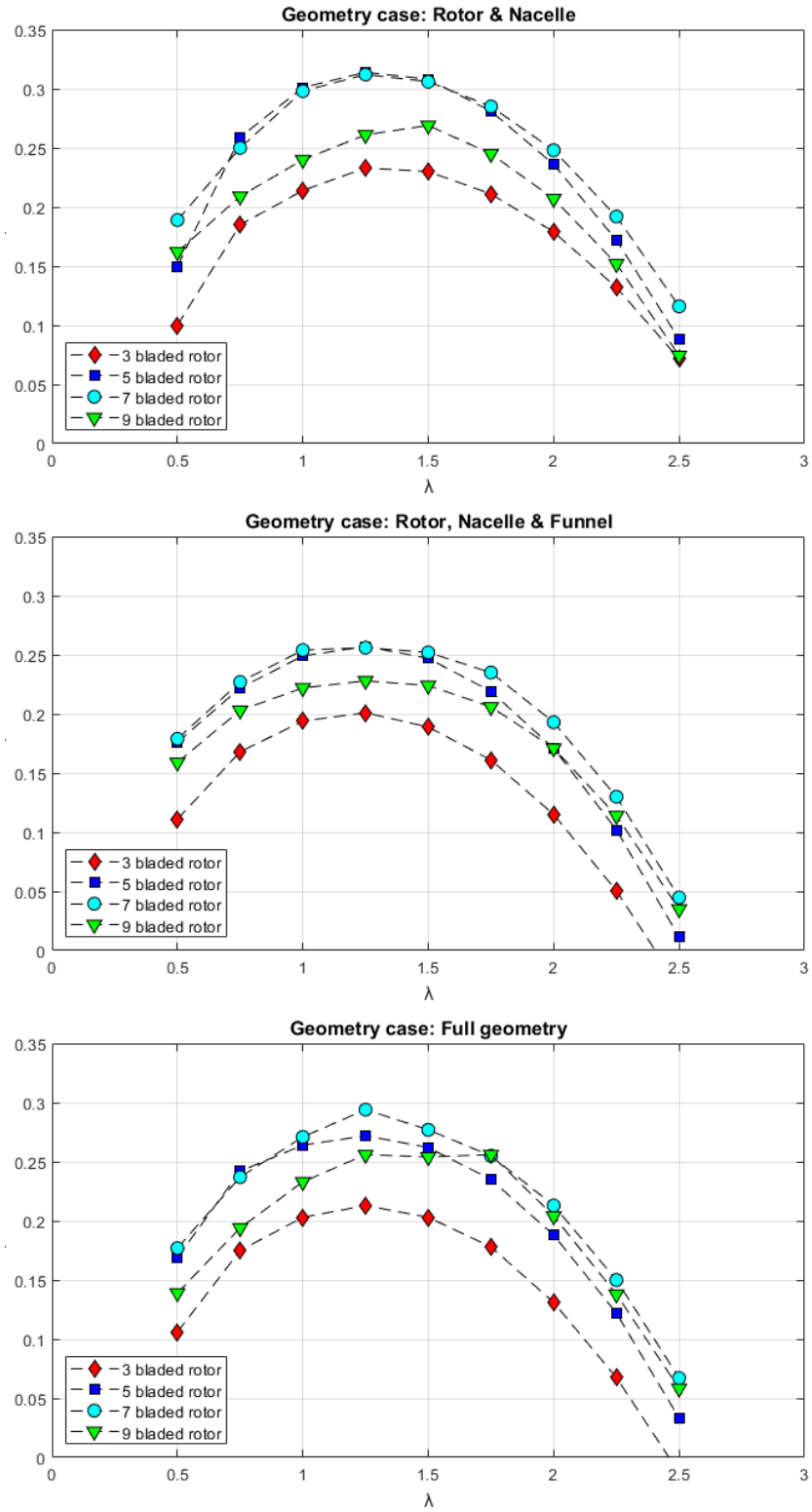

Figure 18: Power coefficient (C_P) vs. tip speed ratio (λ) comparing the number of blades configurations for the rotor and nacelle (top); rotor, nacelle and funnel (middle); and full geometry (bottom)

4.5 Pressure and Velocity Contours of the Flow Field

In this research, three different geometry cases of the SAHT unit were investigated. Since the full geometry configuration is considered as the main content of this research, the contours of velocity and pressure on the horizontal plane monitor coincident with the turbine hub height are presented only for the full geometry case with four different blade configurations. Additionally, to capture the effects of geometry configurations on performance, the pressure and velocity contours for the five bladed configurations are introduced with three different geometry cases.

4.5.1 Pressure Contours on Horizontal Plane Monitor

Pressure contours on the horizontal plane monitor coincident with the turbine hub height are shown in Figure 19 at the operating condition of λ = 1.25. To facilitate a better comparison of these contours, a supporting graph of normalized pressure vs normalized distance is presented in Figure 20 for the central line monitor.

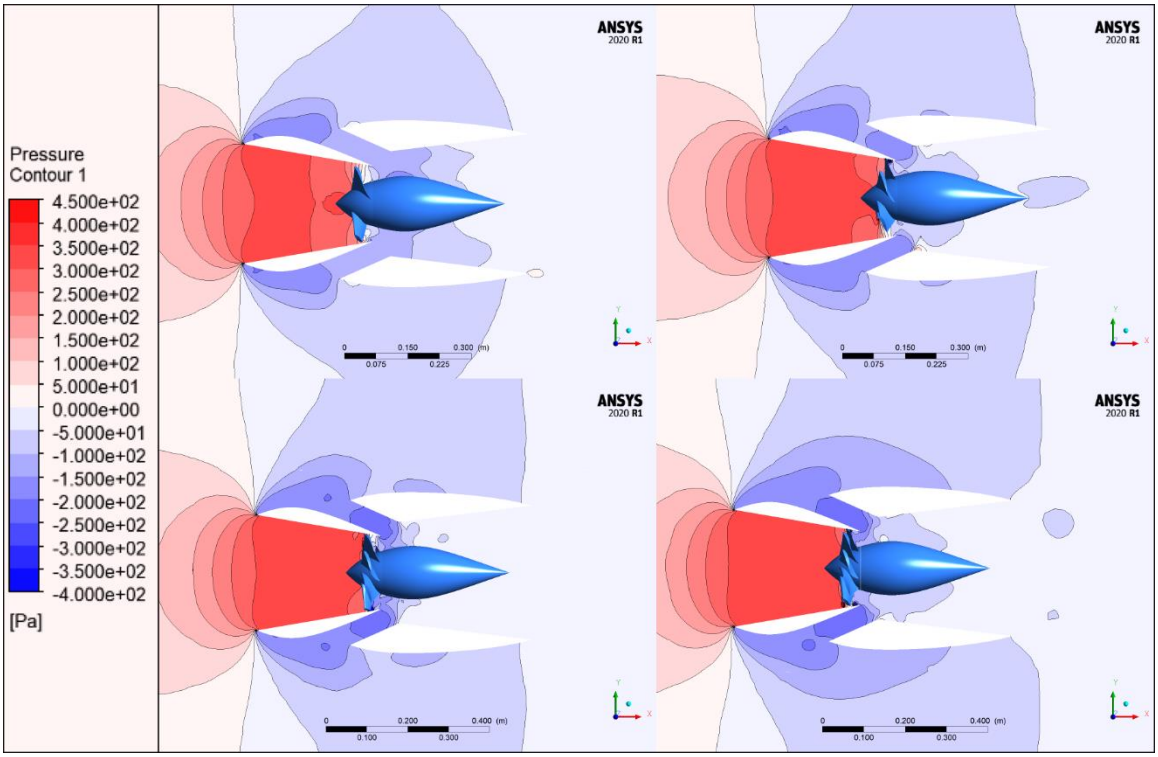

Figure 19: Horizontal plane hub height pressure contours comparing static pressure for different number of blades rotors; Full geometry; λ =1.25

Pressure contours are created with a consistent pressure range of -400 Pa to 450 Pa with an interval of 50 Pa. The pressure was normalized by the pressure value of the point monitor of the three bladed configuration's domain to capture the difference with other blade configurations. The distance coordinate (x) along the x-axis was normalized by the diameter of the funnel opening (D_F). The diameter of the funnel (D_F) was used instead of the typical rotor diameter (D_T) because D_F determines the captured flow area and is used for performance calculations when the funnel is mounted.

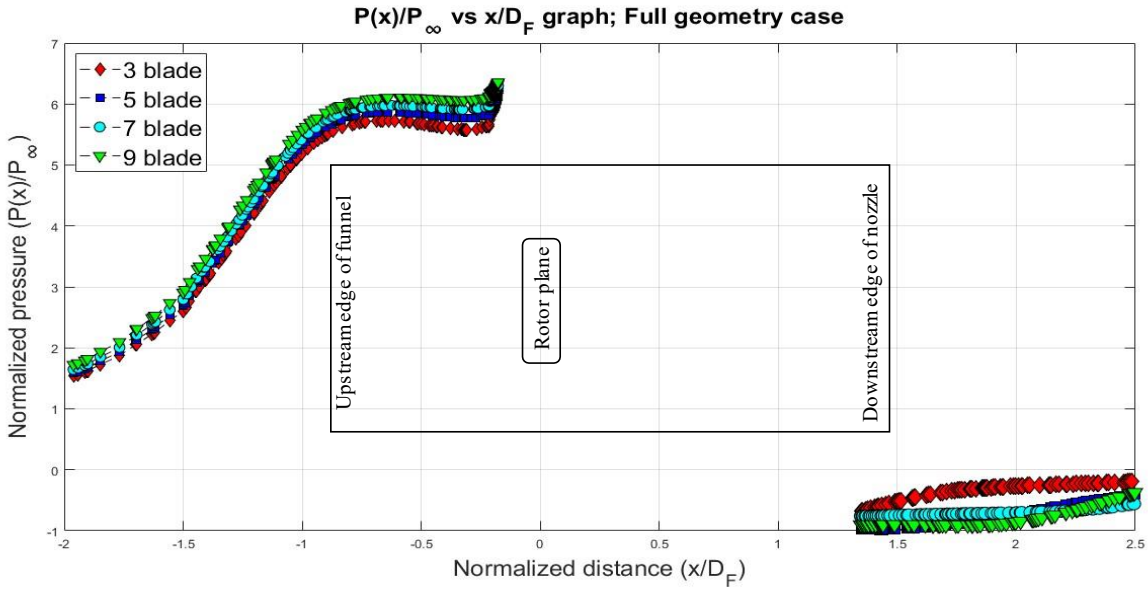

Figure 20: $P_{(x)}/P_{\infty}$ vs x/D_F graphs comparing normalized pressure with normalized distance for rotors with different number of blades; Central line monitor with a range (x, y, z) = (-2D_F, 0, 0) to (2.5D_F, 0, 0); Full geometry; λ = 1.25

By observing the pressure contours (Figure 19) and $P_{(x)}/P_{\infty}$ vs x/D_F graphs (Figure 20) it is clear that immediately upstream of the rotor, the pressure was increasing as the number of blades on the rotor increased.

4.5.2 Velocity Contours on Horizontal Plane Monitor

Figure 21 shows velocity magnitude contours on the horizontal plane monitors while operating at λ = 1.25. Figure 22 shows a supporting graph of the normalized velocity versus normalized distance for the central line monitor to allow for a better comparison of the contours. Velocity contours are drawn using a constant velocity range of 0 m/s to 1.1 m/s and at 0.1 m/s intervals. To capture the difference with other blade configurations, the velocity was normalized by the velocity value of the point monitor of the three bladed configuration's domain. The diameter of the funnel opening (D_F) was used to normalize the distance coordinate (x) along the x-axis.

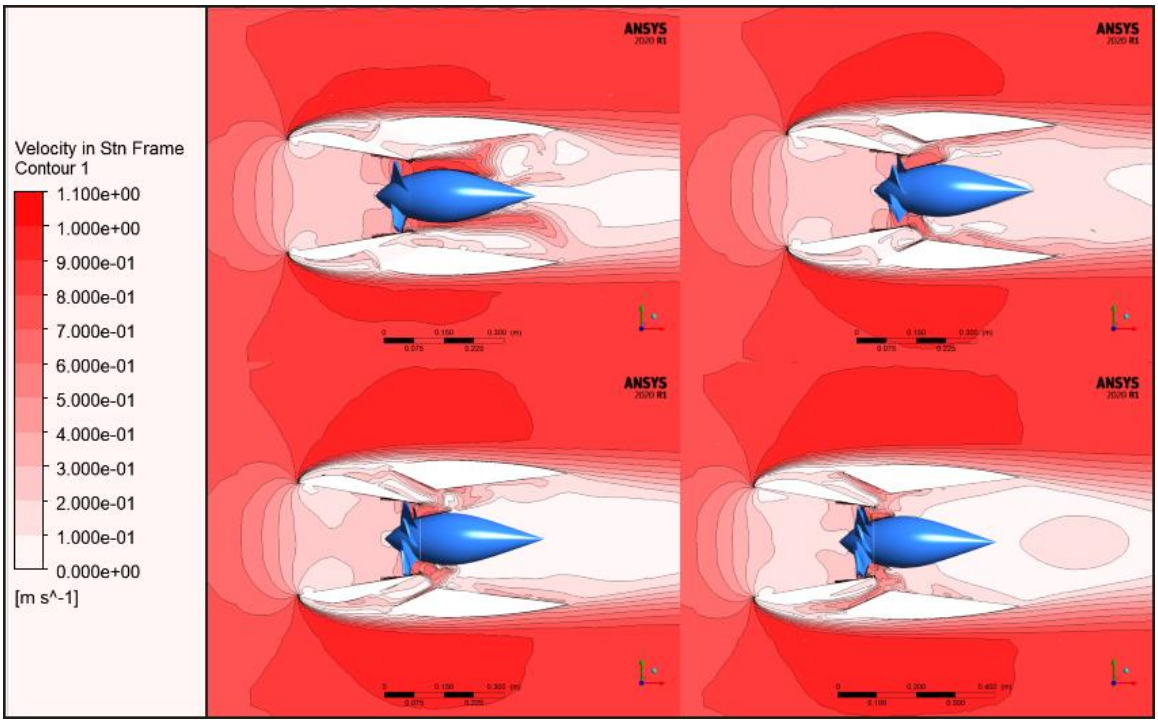

Figure 21: Horizontal plane monitor velocity contours on horizontal plane monitor comparing velocity magnitude for the different number of blades rotors; Full geometry; λ = 1.25.

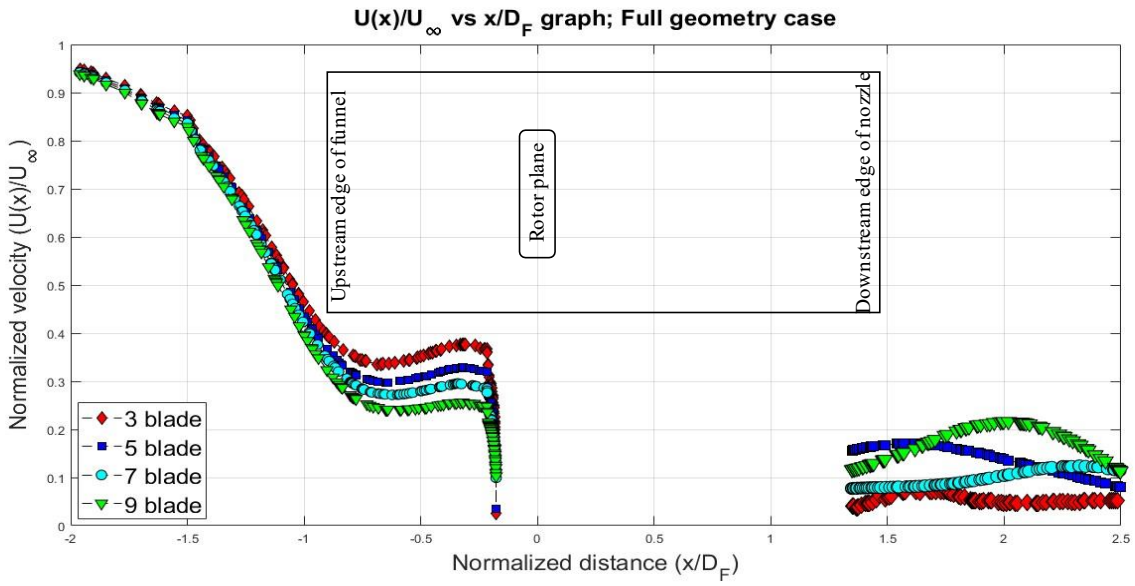

Figure 22: $U_{(x)}/U_{\infty}$ vs x/D_F graphs comparing normalized velocity with normalized distance for different number of blades rotors, Central line monitor with a range (x, y, z) = (-2D_F, 0, 0) to (2.5D_F, 0, 0); Full geometry; λ = 1.25

It is evident from the velocity contours (Figure 21) and $U_{(x)}/U_{\infty}$ vs x/D_F plots (Figure 22) that the velocity was decreasing upstream of the rotor as the number of blades increased. It also gave an impression of flow blocking with an increase in the number of blades and illustrates how the full geometry impacts flow characteristics far upstream of the funnel location.

4.5.3 Pressure Contours with 5 Bladed Configurations

Contours of pressure for three different geometries are introduced in Figure 23 and a normalized pressure graph is provided in Figure 24 to compare the contour effortlessly. Pressure contours (Scale range: -400 Pa to 450 Pa, 50 Pa interval) were drawn for the optimal operating configuration with a five-bladed rotor and at λ = 1.25. The pressure was normalized by the point monitor value of the rotor and nacelle configuration (Figure 24).

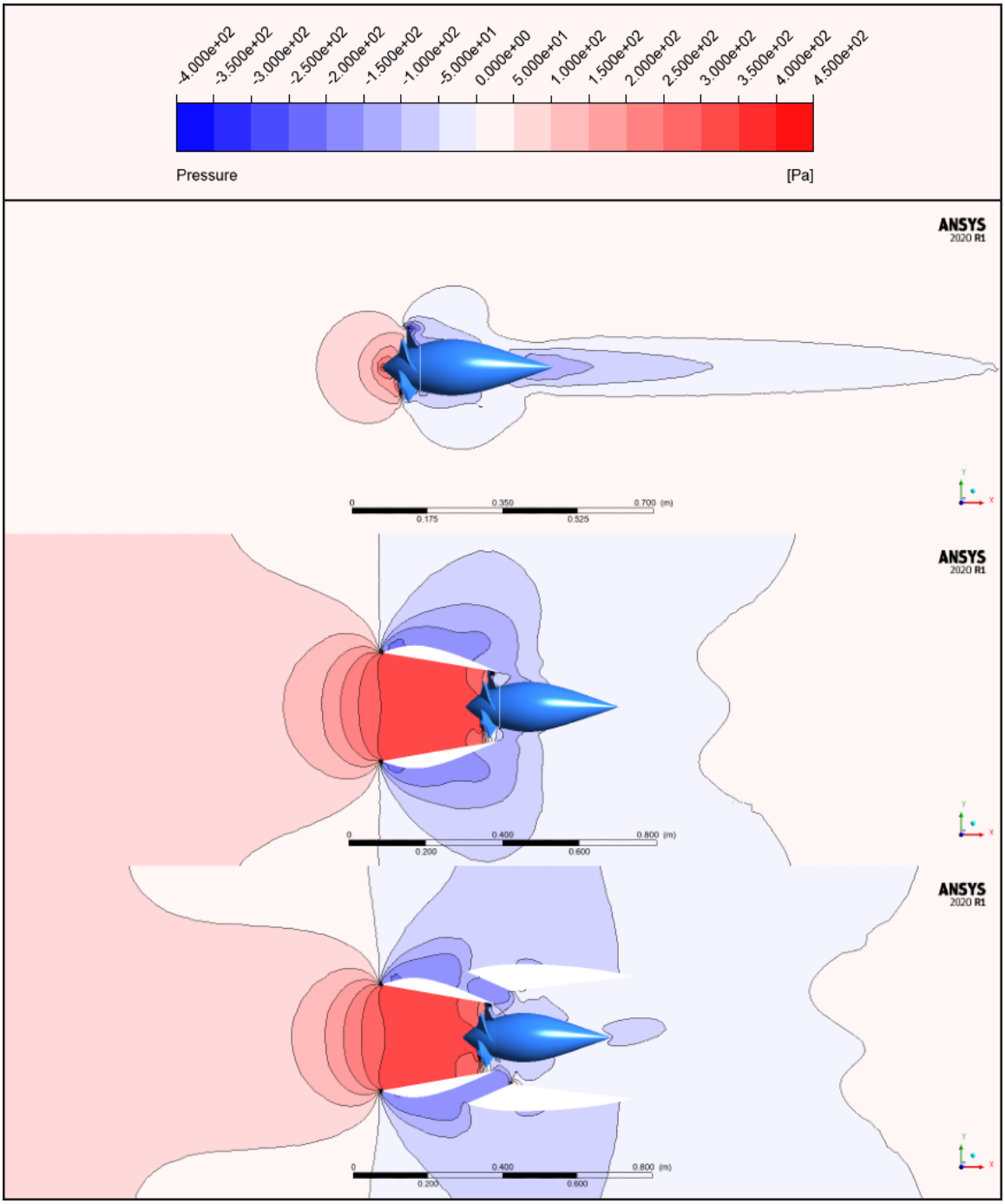

Figure 23: Horizontal plane hub height pressure contours comparing static pressure for different geometry configurations; 5 bladed rotors; λ = 1.25

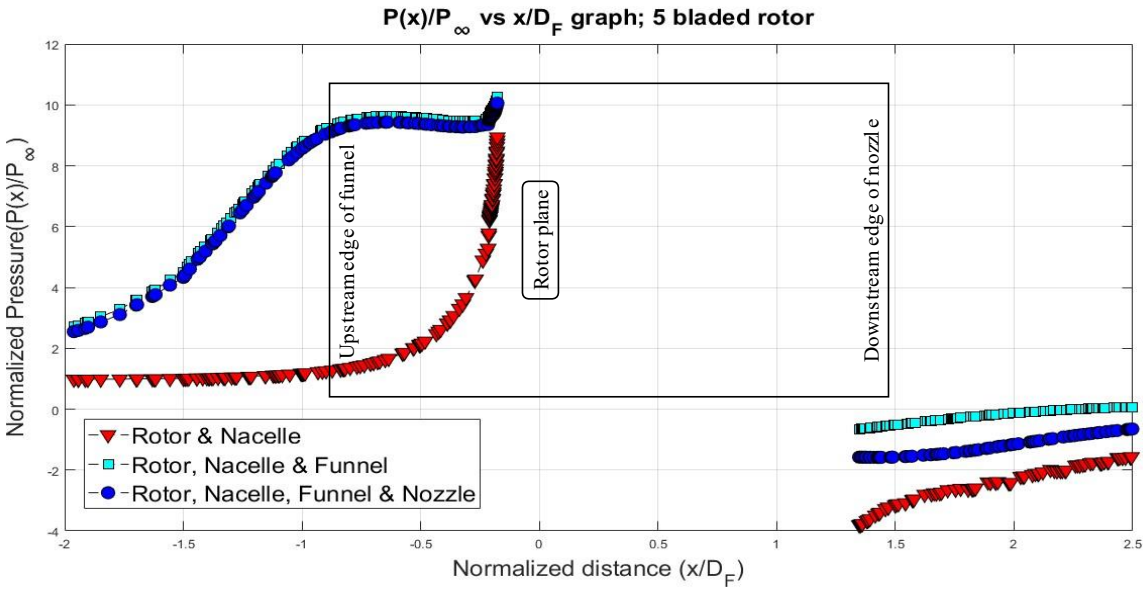

Figure 24: $P_{(x)}/P_{\infty}$ *vs* x/D_F graphs comparing normalized pressure with normalized distance for different geometry configurations; Central line monitor with a range $(x, y, z) = (-2D_F, 0, 0)$ to $(2.5D_F, 0, 0)$; 5 bladed rotor; $\lambda = 1.25$

4.5.4 Velocity Contours with 5 Bladed Configurations

Velocity contours for three different geometries are introduced in Figure 25 with a normalized velocity graph provided in Figure 26 to compare the contours more closely. Velocity contours (scale range: 0 m/s to 1.1 m/s, 0.1 m/s intervals) were also drawn for the optimal operating configuration with a five-bladed rotor and at $\lambda = 1.25$. The velocity was normalized by the point monitor value of the rotor and nacelle configuration.

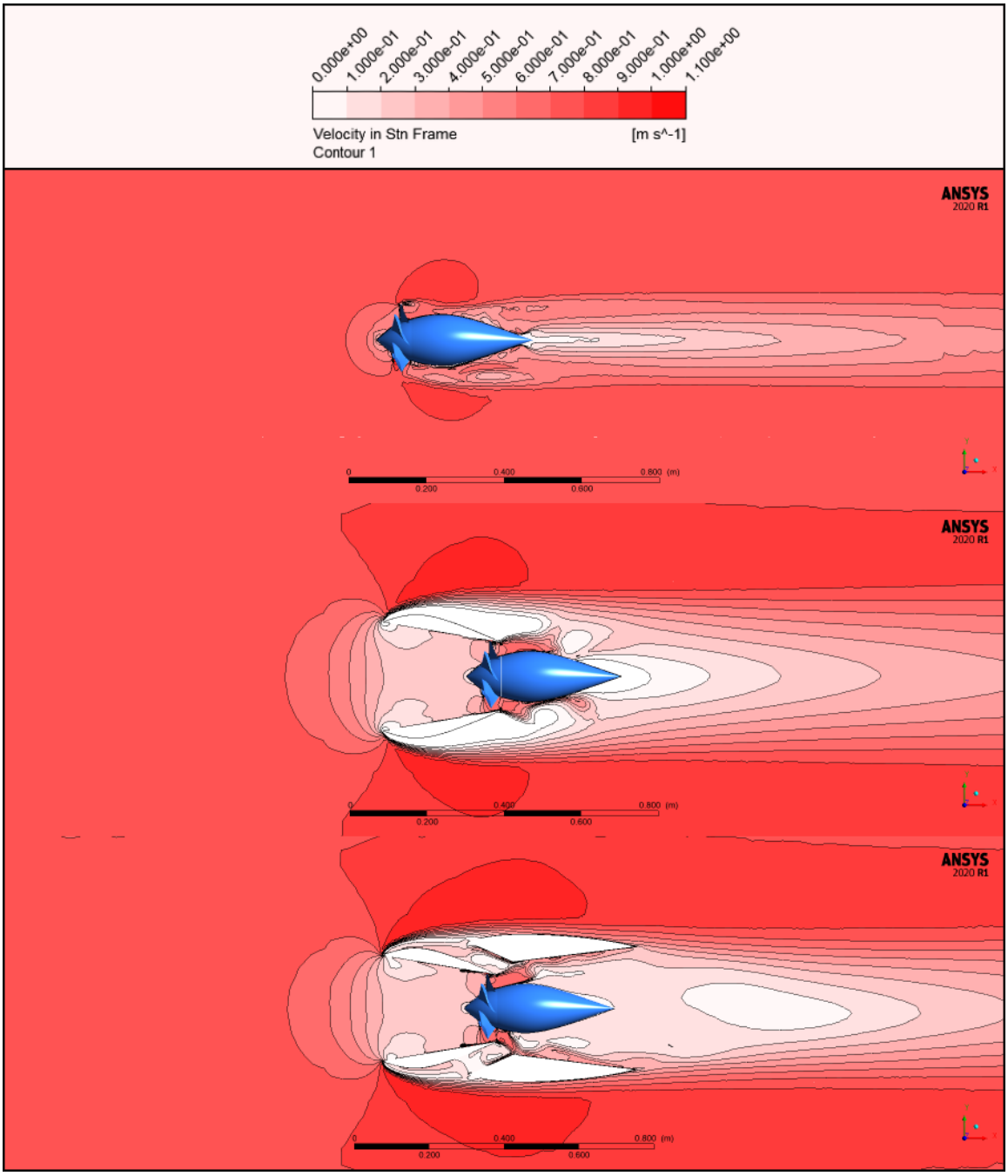

Figure 25: Horizontal plane hub height velocity contours comparing velocity magnitude for different geometry configurations; 5 bladed rotor; λ = 1.25.

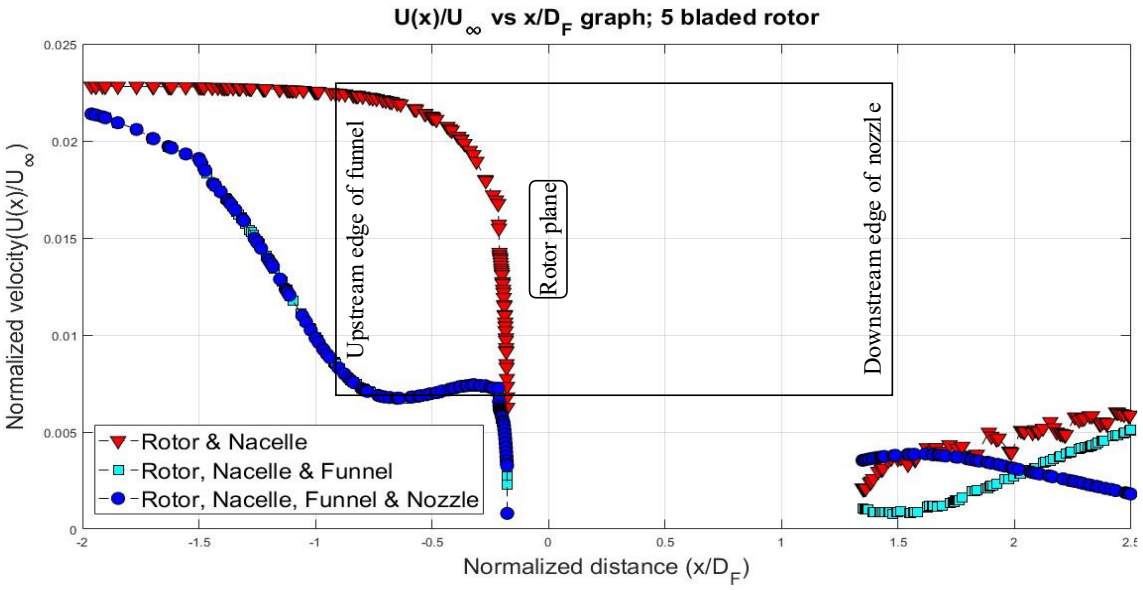

Figure 26: $U_{(x)}/U_{\infty}$ vs x/D_F graphs comparing normalized velocity with normalized distance for different geometry configurations, Central line monitor with a range (x, y, z) = (-2D_F, 0, 0) to (2.5D_F, 0, 0); 5 bladed rotor; λ = 1.25

The minimum pressure and maximum velocity appeared upstream of the rotor with only rotor and nacelle geometry configuration. The pressure is increasing and velocity is decreasing with the inclusion of funnel and nozzle. Thus, the fluid velocity is decreasing through the rotor with the presence of funnel or both funnel and nozzle.

4.6 Turbine Surface Pressure Contours

Surface pressure contours on the five bladed turbine rotors are shown in Figure 27 for three different geometry setups. The pressure contour scale was -800 Pa to 800 Pa with an interval of 50 Pa. Left and right column of Figure 27 represents the high-pressure region and low-pressure region respectively on turbine surface. For each case, local regions on the low-pressure side near the leading edge (rotor and nacelle case) and the blade tips (funnel with and without the nozzle) indicate potential flow separation, possibly locations where cavitation could occur, and a need for a further redesign of the blade geometry.

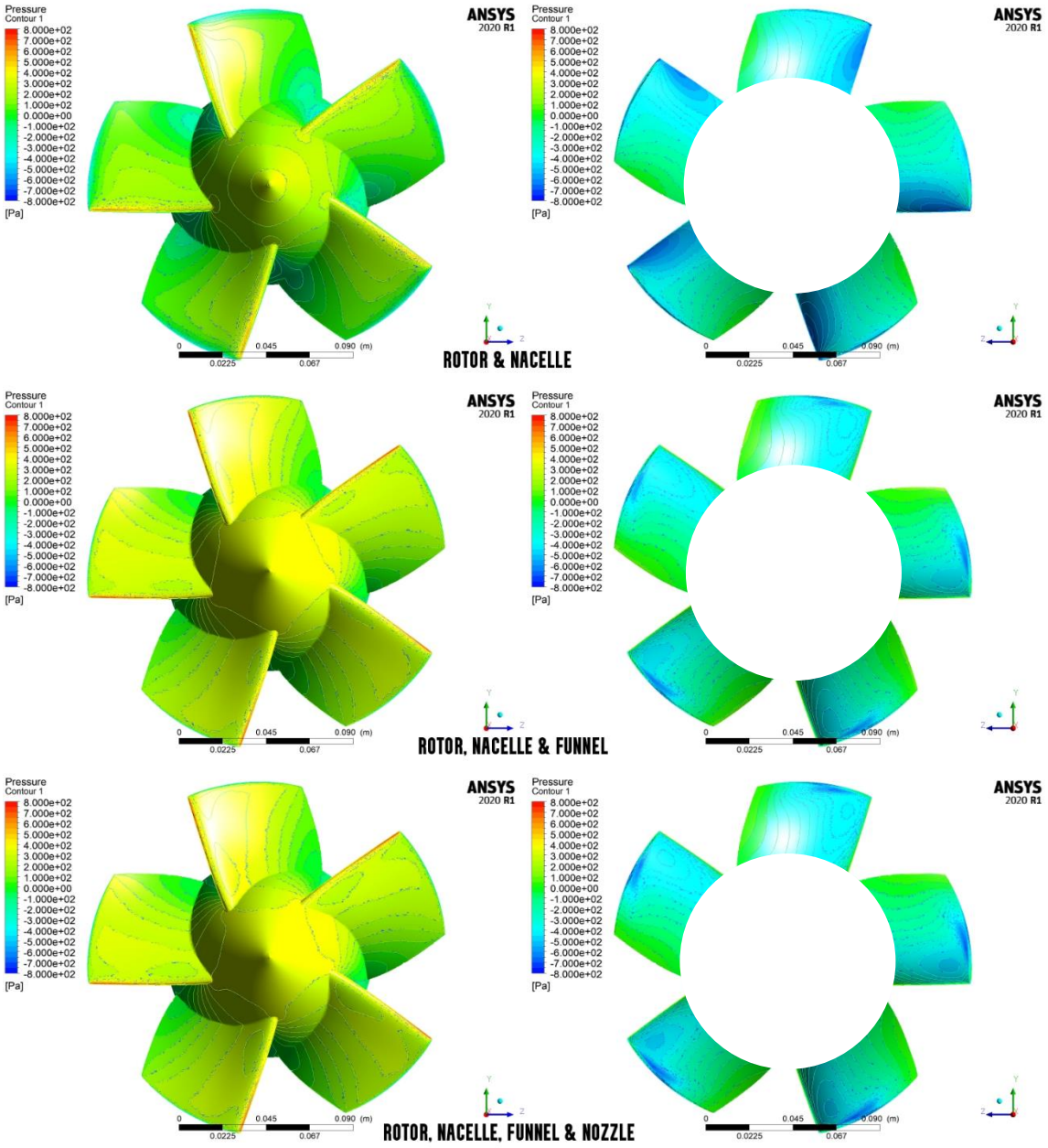

Figure 27: Surface pressure contours; 5 bladed turbines. (left column) The upstream high-pressure side of blades, (right column) downstream low-pressure side of blades. Other cases were omitted for brevity.

4.7 Turbine Surface y^+ Contours

The non-dimensional distance y^+ is frequently used to define the coarseness or fineness of a mesh for a specific flow pattern. In turbulence modeling, determining the correct size of cells near domain barriers and the correct y^+ value is critical to be confirmed for the resolution of turbulent flow near the wall by any specific turbulence model. For example, with ANSYS Fluent, the k-ω SST turbulence model resolves the boundary layer in the viscous sub-layer very close to the wall and requires a y^+ <20 for this model to be suitable for accurate use. For the k-ε turbulence model, the range is typically $20 < y^+ < 200$ to resolve the boundary layer in the log layer which is farther away from the wall than the viscous sublayer. Figure 28 presents the y^+ contours on different rotor configurations for the full geometry case. The maximum y^+ value was 18 for nine bladed rotors, and 22 for the other number of blade configurations. Except for the mesh with nine bladed rotors the y^+ values are slightly higher than the upper limit of allowing y^+ value for the k-ω SST model. For this reason, additional simulations using the five bladed rotor at $\lambda = 1.25$ were explored using the k-ε Realizable turbulence model, which also solves two transport equations same as k-ω turbulence model but here the second transported variable is the rate of dissipation of turbulent kinetic energy. Additionally, the k-ε model predicts well far from the boundaries (wall), and the k-ω model predicts well near the wall. Since the y^+ values are so close to the lower allowable limit of k-ε and upper allowable limit of k-ω SST model, the difference in performance coefficients was negligible (Table 5) and the overall results with k-ω SST turbulence model are taken as an accurate one.

Table 5: Performance coefficients comparison based on different RANS turbulence models.

Performance coefficients	k-ω SST	k-ε Realizable
C_P	0.27	0.26
C_T	0.96	0.93
C_Q	0.22	0.21

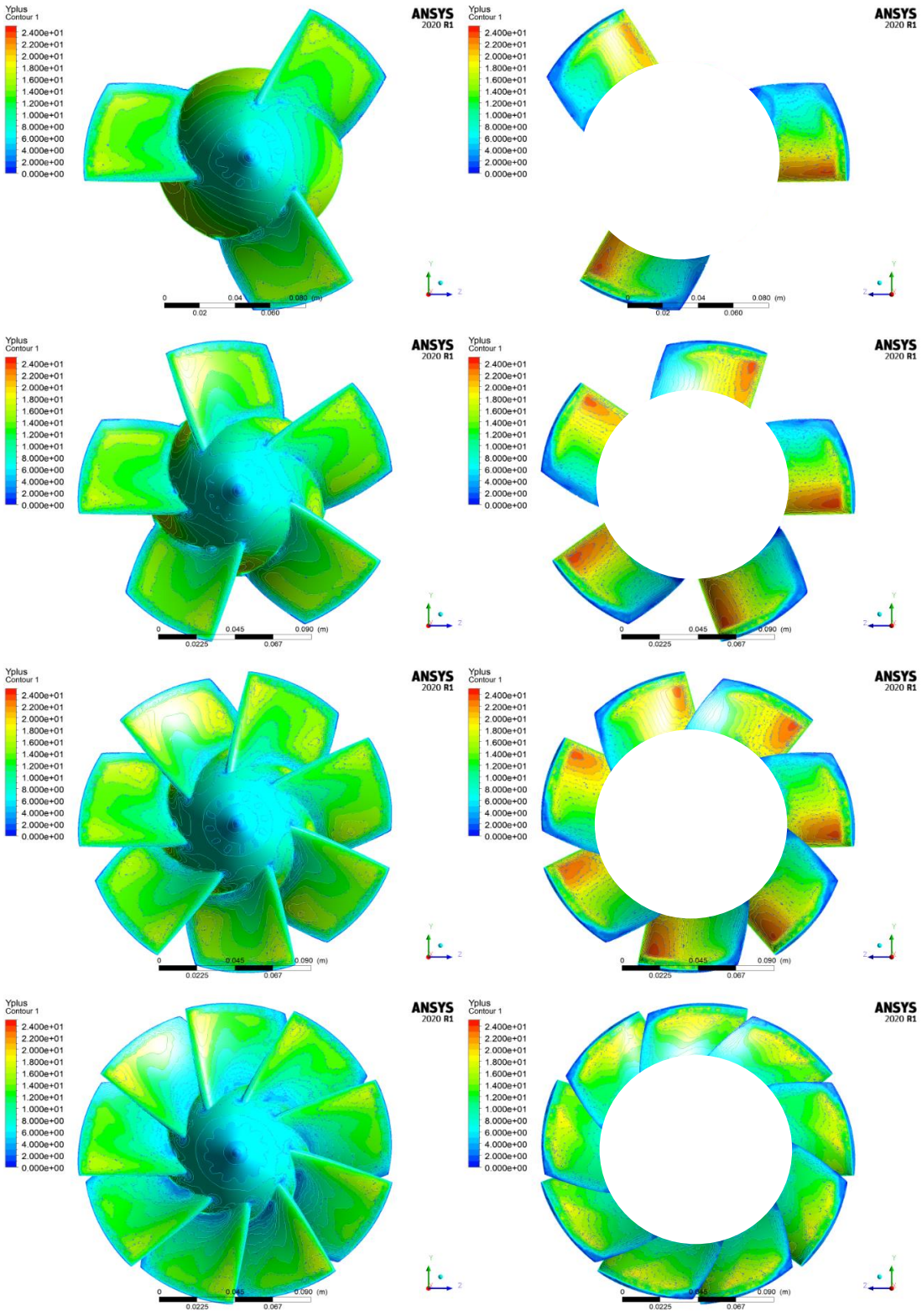

Figure 28: y^+ contours for the different number of blades configurations; Full geometry. (left column) The upstream high-pressure side of blades, (right column) downstream low-pressure side of blades. Other SAHT configurations were omitted for brevity.

Section 5 - Discussion

Under a uniform and constant input velocity of U_∞ = 0.75 m/s and λ ranging from 0.5 to 2.50 with 0.25 intervals, the power performance of the SAHT unit was studied. Only the rotor and nacelle geometry configurations outperformed the rest in terms of performance among the geometry instances. The SAHT unit produced the most power at λ = 1.25 or 95 rpm when compared to other λ values. At λ = 0.5-1.25, the coefficient of power was increasing, then gradually decreasing after λ = 1.25. For all five and seven bladed turbines with the bare rotor and nacelle only, the highest C_P value was 0.31. In terms of manufacturing costs, the five bladed turbines may now be selected as the best option. This study indicates that the SAHT unit's achievable power is substantially lower and not efficient for power production. This is likely due to the design of the funnel and how it captures a larger region of flow or inhibits it from entering the rotor. Instead, the flow freely bypasses the system due to the large pressure build up inside of the funnel.

The thrust coefficient (C_T) pattern is comparable to Borg et al, Batten et al., and Schleicher et al.'s finding [3-5,11, 29]. The initial rise in thrust coefficient is faster for lower tip-speed ratios and peaks at a tip-speed ratio of 0.5 or 0.75, as seen in Figure 9. As tip speed ratios exceed 0.75, the thrust coefficient started dropping, as illustrated in Figure 9 for the different bladed configurations. The thrust was introduced by the axial force on the rotor which is determined by the upstream pressure and downstream suction. The pressure and velocity contours (Figure 19 & 21) on the horizontal hub height plane showed increases in pressure and flow accumulation with a low velocity at the upstream side which also contributed to the flow blocking through the rotor and eventually lower the thrust. These discrepancies are thought to be the result of the higher pitch angle of the rotor blade. Further exploration of the blade design and both funnel and nozzle geometry could clarify thrust characteristics, an important parameter for developers to understand since it impacts turbine foundation structural characteristics, and therefore cost to manufacture.

The flow contours and C_P curves revealed a distinct situation, despite the predicted suction augmentation between the upstream funnel and downstream nozzle gap and improved flow circulation inside of the funnel. The existence of the upstream funnel and

downstream nozzle blocked the flow through the rotor. The sharp leading edge of the upstream funnel separated the flow from its surface (Figure 29). Due to the boundary layer separation on the upstream funnel surface, a high-pressure region was created around the funnel surface. Following Bernoulli's principle, the incoming flow velocity drastically decreased when it entered the funnel and there was no augmentation of flow via the space between funnel and nozzle along with the funnel inside.

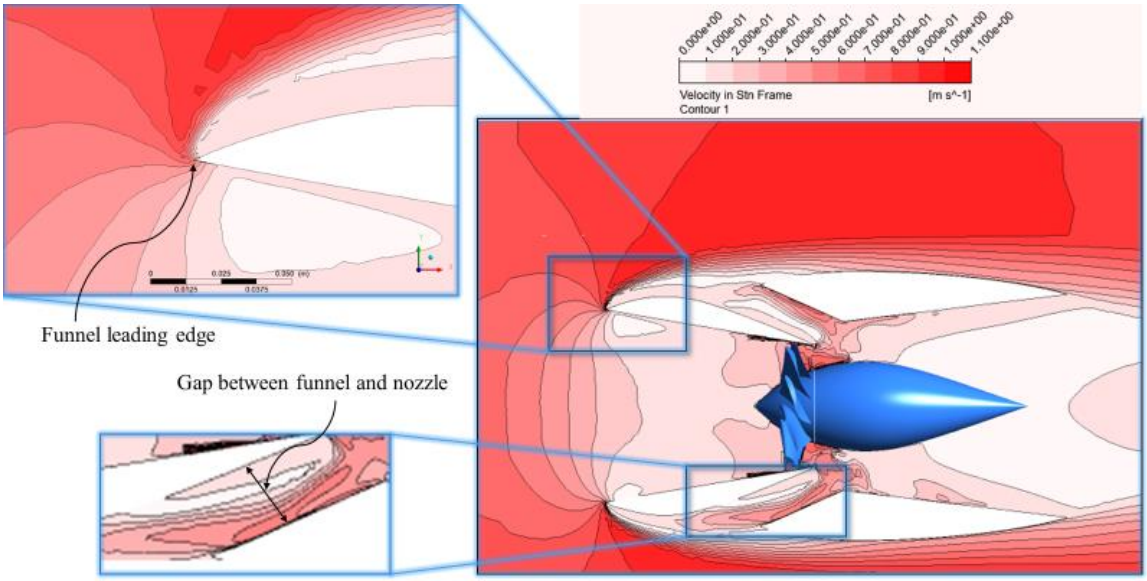

Figure 29: Flow separation by the funnel leading edge.

The flow behind the rotor also decreased due to extracting energy from the flowing water and gradually recovered its velocity after passing the turbulent wake zone behind the rotor. With the presence of the downstream nozzle, it took more distance to recover the flow velocity than without nozzle geometry. This larger wake zone and longer recovery would impact energy availability and production by any additional turbines mounted downstream. Consequently, the addition of a funnel and nozzle as designed for the current SAHT unit had no hydrodynamic and performance gain. In conclusion, with the present design of the SAHT unit and blades profile, the bare rotor and nacelle configuration with five bladed rotor proves to be the superior option to the ducted rotor and nacelle.

Section 6 - Future Research and Recommendations

The original hypothesis by the company SAHT Energy LLC was that the downstream nozzle would cause the flow to accelerate in the channel between the funnel and nozzle, create a low-pressure zone downstream of the rotor as a result of this higher velocity, and use this increased pressure differential to accelerate flow across the rotor plane to increase power production. The CFD study did not support this hypothesis but did provide ideas for future research and recommendations. A major focus of future studies should emphasize a redesign of the funnel and nozzle. The leading edge of the funnel should be rounded similar to traditional airfoils, and the exact internal geometry and angle of attack of the funnel and nozzle need further exploration. This will help prevent flow separation, which as you can see in the images illustrating the flow field, often create a low-velocity wake that reattaches to the turbine geometry downstream of the entrance to the channel between the funnel and nozzle, thereby preventing flow acceleration in that region into the inner nozzle region. Regions of very low pressure on the suction side of the blades shown in Figure 27 indicate that the blade geometry could be explored in the future to further optimize performance and mitigate the possibility of cavitation occurring on the blade surfaces.

Section 7 - Conclusion

This project investigated the SAHT Energy LLC's (Eugene, OR, USA) patented suction augmented hydrokinetic turbine (SAHT) to determine the hydrodynamic and power performance characteristics under various operating conditions. Computational fluid dynamics (CFD) tools explored a range of rotor and turbine configurations to determine if SAHT's patented technology and flow augmenting hypothesis did indeed enhance its performance beyond that of a non-ducted turbine. Results found contradiction with the hypothesized ducted marine hydrokinetic turbine's performance. Other ducted MHK turbines currently being developed produce more power than a non-ducted rotor, yet the studied SAHT unit's performance decreased with the presence of an upstream funnel duct and downstream nozzle that was hypothesized to augment hydrodynamics and greatly enhance power performance.

The existing SAHT unit produced its maximum $C_P = 0.31$ with bare rotor and nacelle configuration for five and seven bladed rotor configurations with a thrust coefficient of $C_T = 0.78$ and 0.89 respectively at a nominal tip-speed ratio of $\lambda = 1.25$. The funnel and nozzle did not beneficially contribute to flow augmentation, but instead, their installation decreased the performance such as with five bladed rotor, the funnel and nozzle installation costs 13% reduction in C_P compared with only rotor and nacelle case. The thrust coefficient was initially increasing at very low λ values and then dropped down gradually after crossing the peak point at $\lambda = 0.5$ or 0.75. The torque coefficient followed the same trend as the thrust coefficient, but it was decreasing sharply as tip speed ratios increased.

The sudden flow separation at the sharp point leading edge of the upstream funnel was a crucial observation, and it should be modified as future work to prevent the flow separation. This flow separation was shown to envelop the entrance to the gap between the funnel and nozzle, which the developer initially thought would introduce additional accelerated flow into the near-wake region of the rotor. Additionally, further exploration of a lower pitch angle rotor is proposed, in addition to validation of CFD modeling with a scaled model physical study in the flume (currently in progress). Prior to entering the

market, a cost analysis of the SAHT unit's manufacture and installation is also highly suggested.

To summarize, the existing SAHT will not benefit from the hydrodynamic advantages of flow augmentation, and a redesign of the unit's components will be required as future work.

Section 8 - References

1. Allsop, Steven, Peyrard, C., Thies, R., Boulougouris, E., and Harrison, G. "Hydrodynamic analysis of a ducted, open centre tidal stream turbine using blade element momentum theory." Ocean Engineering 141 (2017): 531-542.

2. Asmus, P., and Wheelock, C. "Hydrokinetic and ocean energy: renewable power generation from ocean wave, tidal stream, river hydrokinetic, ocean current, and ocean thermal technologies." Boulder, USA: Pike Research LLC (2009).

3. Batten, W., Bahaj, A., Molland, A., and Chaplin, J. "Hydrodynamics of marine current turbines." Renewable energy 31, no. 2 (2006): 249-256.

4. Batten, W., Bahaj, A., Molland, A., and Chaplin, J. "The prediction of the hydrodynamic performance of marine current turbines." Renewable energy 33, no. 5 (2008): 1085-1096.

5. Batten, W., Bahaj, A., Molland, A., and Chaplin, J. and Sustainable Energy Research Group. "Experimentally validated numerical method for the hydrodynamic design of horizontal axis tidal turbines." Ocean engineering 34, no. 7 (2007): 1013-1020.

6. Bernad, Sandor, Andrei, G., Sanda G., Romeo, R., and Ioan, A. "Flow investigations in Achard turbine." Proceedings of the Romanian Academy 9, no. 2 (2008): 000.

7. Bergey, Karl H. "The Lanchester-Betz limit (energy conversion efficiency factor for windmills)." Journal of Energy 3, no. 6 (1979): 382-384.

8. Bilgen, Selcuk, Sedat, K., Abdullah, K., Ahmet, S., and Kamil, K. "Global warming and renewable energy sources for sustainable development: a case study in Turkey." Renewable and sustainable energy reviews 12, no. 2 (2008): 372-396.

9. Blackaby, N. (November 22, 2018). *Joint venture to launch French tidal energy project*. Renewable Energy World. https://www.renewableenergyworld.com/storage/joint-venture-to-launch-french-tidal-energy-project/#gref

10. Bontempo, R., and Manna, M. "Performance analysis of open and ducted wind turbines." Applied Energy 136 (2014): 405-416.

11. Borg, Mitchell, G., Xiao, Q., Allsop, S., Incecik, A., and Peyrard, C., "A numerical performance analysis of a ducted, high-solidity tidal turbine." Renewable Energy 159 (2020): 663-682.

12. Boyle, Godfrey. Renewable energy. 2004.

13. Harper, P., Hallett, H., Fleming, A., and Dawson, M. "Advanced fibre-reinforced composites for marine renewable energy devices." In Marine Applications of Advanced Fibre-Reinforced Composites, pp. 217-232. Woodhead Publishing, 2016.

14. Herzog, Antonia, V., Timothy E., L., and Daniel M., K. "Renewable energy sources." Encyclopedia of life support systems (EOLSS). Forerunner Volume-'Perspectives and overview of life support systems and sustainable development 76 (2001).

15. Kaltschmitt, Martin, Wolfgang, S., and Andreas, W., eds. Renewable energy: technology, economics and environment. Springer Science & Business Media, 2007.

16. Khan, M. J., Bhuyan, G., Iqbal, M. T., and Quaicoe, J. E. "Hydrokinetic energy conversion systems and assessment of horizontal and vertical axis turbines for river and tidal applications: A technology status review." Applied energy 86, no. 10 (2009): 1823-1835.

17. Khan, M. J., Iqbal, M. T., and Quaicoe, J. E. "River current energy conversion systems: Progress, prospects and challenges." Renewable and Sustainable Energy Reviews 12, no. 8 (2008): 2177-2193.

18. Kirke, Brian. "Developments in ducted water current turbines." Tidal paper 25-04 (2006).

19. Laws, Nicholas, D., and Brenden P., E. "Hydrokinetic energy conversion: Technology, research, and outlook." Renewable and Sustainable Energy Reviews 57 (2016): 1245-1259.

20. LiVecchi, A., A. Copping, D. Jenne, A. Gorton, R. Preus, G. Gill, R. Robichaud, R. Green, S. Geerlofs, S. Gore, D. Hume, W. McShane, C. Schmaus, H. Spence. 2019.

Powering the Blue Economy; Exploring Opportunities for Marine Renewable Energy in Maritime Markets. U.S. Department of Energy, Office of Energy Efficiency and Renewable Energy. Washington, D.C.

21. Marine Energy Resource Assessment and Characterization. Water Power Technologies Office. https://www.energy.gov/eere/water/marine-energy-resource-assessment-and-characterization

22. Pachauri, Shonali. An energy analysis of household consumption: Changing patterns of direct and indirect use in India. Vol. 13. Springer Science & Business Media, 2007.

23. Power, V. (October 22, 2020). Three Verdant Power Tidal Turbines Deployed in New York City's East River. Verdant Power. https://www.verdantpower.com/news-rite-install-10-22-20

24. Previsic, Mirko, Moreno, A., Bedard, R., Polagye, B., Collar, C., Lockard, D., Toman, W., et al. "Hydrokinetic energy in the United States—resources, challenges and opportunities." In Proceedings of 8th European Wave Tidal Energy Conference, pp. 76-84. 2009.

25. Punys, Petras, Adamonyte, I., Kvaraciejus, A., Martinaitis, E., Vyciene, G., and Kasiulis, E. "Riverine hydrokinetic resource assessment. A case study of a lowland river in Lithuania." Renewable and Sustainable Energy Reviews 50 (2015): 643-652.

26. RER Hydro. URL (2014). http://www.rerhydro.com/turbines/trek/

27. Riegler, Gerold. "Principles of energy extraction from a free stream by means of wind turbines." Wind Engineering (1983): 115-126.

28. Saini, Gaurav, and Saini, R. "A review on technology, configurations, and performance of cross-flow hydrokinetic turbines." International Journal of Energy Research 43, no. 13 (2019): 6639-6679.

29. Schleicher, W., Riglin, J., and Oztekin, A. "Numerical characterization of a preliminary portable micro-hydrokinetic turbine rotor design." Renewable Energy 76 (2015): 234-241.

30. SIMEC Atlantis Energy Tidal Turbines. SIMEC Atlantis. 2019. https://simecatlantis.com/services/turbines/

31. Stelzenmuller, Nickolas, K., "Marine hydrokinetic turbine array performance and wake characteristics." PhD diss., 2014

32. Tampier, Gonzalo, Troncoso, C., and Zilic, F., "Numerical analysis of a diffuser-augmented hydrokinetic turbine." Ocean engineering 145 (2017): 138-147.

33. Tukker, Arnold, Martin, C., Carlo, V., Eivind S., and Maj, A., eds. System innovation for sustainability 1: Perspectives on radical changes to sustainable consumption and production. Routledge, 2017.

34. Vanek, Francis, M., Louis, A., and Largus, A,. Energy systems engineering: evaluation and implementation. McGraw-Hill Education, 2016.

35. Yuce, Ishak, M., and Muratoglu, A. "Hydrokinetic energy conversion systems: A technology status review." Renewable and Sustainable Energy Reviews 43 (2015): 72-82.

Section 9 - Appendices

9.1 Detailed Tables of Numerical Results

Table 6: Tabulated summary of performance testing for SAHT with only the rotor and nacelle test case

	Flow Conditions				Number of Blades: 3					Number of Blades: 5					Number of Blades: 7					Number of Blades: 9				
					Performance					Performance					Performance					Performance				
	U (m/s)	TSR (λ)	ω (rad/s)	I_U (%)	τ (Nm)	F (N)	C_P	C_T	C_Q	τ (Nm)	F (N)	C_P	C_T	C_Q	τ (Nm)	F (N)	C_P	C_T	C_Q	τ (Nm)	F (N)	C_P	C_T	C_Q
Rotor &Nacelle	0.75	0.50	3.97	5	0.15	3.97	0.10	0.50	0.20	0.22	5.97	0.15	0.76	0.30	0.28	7.91	0.19	1.00	0.38	0.24	8.17	0.16	1.04	0.32
	0.75	0.75	5.95	5	0.18	4.48	0.19	0.57	0.25	0.26	6.55	0.26	0.83	0.34	0.25	7.71	0.25	0.98	0.33	0.21	7.81	0.21	0.99	0.28
	0.75	1.00	7.94	5	0.16	4.27	0.21	0.54	0.21	0.22	6.46	0.30	0.82	0.30	0.22	7.52	0.30	0.96	0.30	0.18	7.52	0.24	0.95	0.24
	0.75	1.25	9.92	5	0.14	4.15	0.23	0.53	0.19	0.19	6.12	0.31	0.78	0.25	0.19	7.03	0.31	0.89	0.25	0.16	7.28	0.26	0.92	0.21
	0.75	1.50	11.90	5	0.11	3.86	0.23	0.49	0.15	0.15	5.68	0.31	0.72	0.21	0.15	6.47	0.31	0.82	0.20	0.13	6.98	0.27	0.89	0.18
	0.75	1.75	13.89	5	0.09	3.48	0.21	0.44	0.12	0.12	5.15	0.28	0.65	0.16	0.12	5.92	0.29	0.75	0.16	0.10	6.45	0.24	0.82	0.14
	0.75	2.00	15.87	5	0.07	3.07	0.18	0.39	0.09	0.09	4.55	0.24	0.58	0.12	0.09	5.38	0.25	0.68	0.12	0.08	5.98	0.21	0.76	0.10
	0.75	2.25	17.86	5	0.04	2.62	0.13	0.33	0.06	0.06	3.89	0.17	0.49	0.08	0.06	4.82	0.19	0.61	0.09	0.05	5.50	0.15	0.70	0.07
	0.75	2.50	19.84	5	0.02	2.15	0.07	0.27	0.03	0.03	3.19	0.09	0.40	0.04	0.03	4.23	0.12	0.54	0.05	0.02	4.99	0.07	0.63	0.03

Table 7: Tabulated summary of performance testing for SAHT with the rotor, nacelle, and funnel test case

	Flow Conditions				Number of Blades: 3					Number of Blades: 5					Number of Blades: 7					Number of Blades: 9				
					Performance					Performance					Performance					Performance				
	U (m/s)	TSR (λ)	ω (rad/s)	I_U (%)	τ (Nm)	F (N)	C_P	C_T	C_Q	τ (Nm)	F (N)	C_P	C_T	C_Q	τ (Nm)	F (N)	C_P	C_T	C_Q	τ (Nm)	F (N)	C_P	C_T	C_Q
Rotor, Nacelle & Funnel	0.75	0.50	3.97	5	0.16	5.57	0.11	0.71	0.22	0.26	8.27	0.18	1.05	0.35	0.27	10.2	0.18	1.29	0.36	0.24	11.2	0.16	1.43	0.32
	0.75	0.75	5.95	5	0.17	5.71	0.17	0.73	0.22	0.22	8.03	0.22	1.02	0.30	0.23	9.77	0.23	1.24	0.30	0.20	10.8	0.20	1.38	0.27
	0.75	1.00	7.94	5	0.14	5.67	0.19	0.72	0.19	0.18	7.77	0.25	0.99	0.25	0.19	9.33	0.25	1.18	0.25	0.17	10.2	0.22	1.29	0.22
	0.75	1.25	9.92	5	0.12	5.50	0.20	0.70	0.16	0.15	7.41	0.26	0.94	0.21	0.15	8.68	0.26	1.10	0.20	0.14	9.61	0.23	1.22	0.18
	0.75	1.50	11.90	5	0.09	5.16	0.19	0.65	0.13	0.12	6.89	0.25	0.87	0.16	0.12	8.15	0.25	1.03	0.17	0.11	9.11	0.22	1.16	0.15
	0.75	1.75	13.89	5	0.07	4.67	0.16	0.59	0.09	0.09	6.26	0.22	0.79	0.13	0.10	7.60	0.24	0.96	0.13	0.09	8.60	0.21	1.09	0.12
	0.75	2.00	15.87	5	0.04	4.06	0.11	0.51	0.06	0.06	5.52	0.17	0.70	0.09	0.07	6.86	0.19	0.87	0.10	0.06	8.04	0.17	1.02	0.09
	0.75	2.25	17.86	5	0.02	3.36	0.05	0.43	0.02	0.03	4.70	0.10	0.60	0.05	0.04	6.08	0.13	0.77	0.06	0.04	7.40	0.11	0.94	0.05
	0.75	2.50	19.84	5	-0.01	2.62	-0.03	0.33	-0.01	0.00	3.84	0.01	0.49	0.00	0.01	5.25	0.04	0.67	0.02	0.01	6.71	0.03	0.85	0.01

Table 8: Tabulated summary of performance testing for SAHT with the full geometry test case

	Flow Conditions				Number of Blades: 3					Number of Blades: 5					Number of Blades: 7					Number of Blades: 9				
					Performance					Performance					Performance					Performance				
	U (m/s)	TSR (λ)	ω (rad/s)	I_U (%)	τ (Nm)	F (N)	C_P	C_T	C_Q	τ (Nm)	F (N)	C_P	C_T	C_Q	τ (Nm)	F (N)	C_P	C_T	C_Q	τ (Nm)	F (N)	C_P	C_T	C_Q
Full Geometry	0.75	0.50	3.97	5	0.16	5.47	0.11	0.69	0.21	0.25	7.98	0.17	1.01	0.34	0.26	10.0	0.18	1.28	0.35	0.21	10.2	0.14	1.30	0.28
	0.75	0.75	5.95	5	0.17	5.77	0.17	0.73	0.23	0.24	8.34	0.24	1.06	0.32	0.24	9.99	0.24	1.27	0.32	0.19	10.5	0.19	1.33	0.26
	0.75	1.00	7.94	5	0.15	5.75	0.20	0.73	0.20	0.20	7.96	0.26	1.01	0.26	0.20	9.63	0.27	1.22	0.27	0.17	10.4	0.23	1.32	0.23
	0.75	1.25	9.92	5	0.13	5.59	0.21	0.71	0.17	0.16	7.58	0.27	0.96	0.22	0.18	9.30	0.29	1.18	0.24	0.15	10.2	0.26	1.30	0.21
	0.75	1.50	11.90	5	0.10	5.27	0.20	0.67	0.14	0.13	7.04	0.26	0.89	0.17	0.14	8.51	0.28	1.08	0.18	0.13	9.65	0.25	1.23	0.17
	0.75	1.75	13.89	5	0.08	4.81	0.18	0.61	0.10	0.10	6.41	0.24	0.81	0.13	0.11	7.82	0.25	0.99	0.15	0.11	9.43	0.26	1.20	0.15
	0.75	2.00	15.87	5	0.05	4.19	0.13	0.53	0.07	0.07	5.68	0.19	0.72	0.09	0.08	7.09	0.21	0.90	0.11	0.08	8.51	0.20	1.08	0.10
	0.75	2.25	17.86	5	0.02	3.50	0.07	0.44	0.03	0.04	4.89	0.12	0.62	0.05	0.05	6.29	0.15	0.80	0.07	0.05	7.70	0.14	0.98	0.06
	0.75	2.50	19.84	5	0.00	2.76	-0.01	0.35	-0.01	0.01	4.04	0.03	0.51	0.01	0.02	5.47	0.07	0.69	0.03	0.02	6.98	0.06	0.89	0.02